

# Energy-efficient and high-precision control of hydraulic robots

Janne Koivumäki <sup>a,\*</sup>, Wen-Hong Zhu <sup>b</sup>, Jouni Mattila <sup>a</sup>

<sup>a</sup> Tampere University of Technology, Laboratory of Automation and Hydraulics, P.O. Box 589, FIN-33101 Tampere, Finland

<sup>b</sup> Canadian Space Agency, 6767, Route de l'Aéroport, Longueuil (St-Hubert), QC, Canada, J3Y 8Y9

## ARTICLE INFO

### Keywords:

Hydraulic robots  
Nonlinear control  
Stability analysis  
Independent metering  
SMISMO control  
Energy efficiency

## ABSTRACT

In addition to *high-precision* closed-loop control performance, *energy efficiency* is another vital characteristic in field-robotic hydraulic systems as energy source(s) must be carried on board in limited space. This study proposes an energy-efficient and high-precision closed-loop controller for the highly nonlinear hydraulic robotic manipulators. The proposed method is twofold: 1) A possibility for energy consumption reduction is realized by using a separate meter-in separate meter-out (SMISMO) control set-up, enabling an independent metering (pressure control) of each chamber in hydraulic actuators. 2) A novel subsystem-dynamics-based and modular controller is designed for the system actuators, and it is integrated to the previously designed state-of-the-art controller for multiple degrees-of-freedom (*n*-DOF) manipulators. Stability of the overall controller is rigorously proven. The comparative experiments with a three-DOF redundant hydraulic robotic manipulator (with a payload of 475 kg) demonstrate that: 1) It is possible to design the triple objective of high-precision *piston position*, *piston force* and *chamber pressure* trackings for the hydraulic actuators. 2) In relation to the previous SMISMO-control methods, unprecedented motion and chamber pressure tracking performances are reported. 3) In comparison to the *state-of-the-art motion tracking controller* with a conventional energy-inefficient servovalve control, the actuators' energy consumption is reduced by 45% without noticeable motion control (position-tracking) deterioration.

## 1. Introduction

Due to hydraulic actuators' many practical advantages like simplicity, robustness, low cost, and large power-to-weight ratio, they have been used for decades in a variety of off-highway machines (e.g., agricultural, construction, forestry, and mining machines). Nowadays, these machines comprise a huge global industrial sector; in 2016, the construction business alone sold 700,000 units of construction machines (Gribbins, 2016), whereas the projected sell in 2019 for the thriving industrial robots is approximately 400,000 units (International Federation of Robotics (IFR), 2017). Due to present aspirations to increase productivity and to lower operating costs, we are heading to a future where these conventional working machines are becoming field-robotic systems, requiring minimal human supervision. Indeed, it is projected that: (1) robotics technology markets will grow substantially in the coming decade (EU Robotics, 2014), and (2) the advent of robotics will revolutionize the (hydraulic) heavy-duty machine industry (Mattila et al., 2017), similarly as is currently happening, e.g., in traffic and the car industry (Daily et al., 2017). In fact, the first commercial semiautonomous products for hydraulic heavy-duty machines are already available in the market, e.g., HIAB crane tip control (HIAB, 2017) for loader cranes and John Deere intelligent boom control (John Deere, 2013) for forest machines. Also, in advanced hydraulic robotic

systems, an extensive academic research is ongoing for heavy-duty machines (Hutter et al., 2017; Koivumäki & Mattila, 2015a,b, 2017a; Mattila et al., 2017) and for legged robots (Boaventura et al., 2015; Hyon et al., 2017a; Koivumäki et al., 2017; Kuindersma et al., 2016; Rong et al., 2012; Semini et al., 2015, 2017).

*Energy efficiency* of ambulatory robotic systems has become an important topic in the recent years (Nurmi & Mattila, 2017; Seok et al., 2015; Xi et al., 2016). In hydraulic systems, energy efficiency has remained one of the most important unsolved challenges (Mattila et al., 2017). Indeed, the aforementioned academic hydraulic robotic systems are all fundamentally energy inefficient due to the use of a conventional energy-inefficient (servo)valve control; see Fig. 1(a). In stationary applications, energy efficiency can be a secondary design objective. However, the situation is different in ambulatory robotic systems where energy sources must be carried on board in limited space (Mattila et al., 2017). A good example of energy inefficient machine is the hydraulic excavator, whose total energy efficiency can be as low as 10%, contributing to approximately 60% of all the construction machinery CO<sub>2</sub> emissions (Vukovic et al., 2017). Today, strict administrative regulations demand energy consumption and CO<sub>2</sub> emissions reductions for the industry; see China's 13th five-year plan (Government of China, 2017).

\* Corresponding author.

E-mail address: [janne.koivumaki@tut.fi](mailto:janne.koivumaki@tut.fi) (J. Koivumäki).

and the new European Union directive for energy efficiency (European Commission, 2012).

In addition to energy efficiency, *high-precision motion* and *force tracking* controls are vital functionalities for robotic systems. However, designing them for hydraulic (robotic) systems is a well-known challenge due to the significant nonlinearities.<sup>1</sup> To address the nonlinearities, nonlinear model-based (NMB) control methods<sup>2</sup> are shown to provide a superior control performance in relation to other control methods (Bech et al., 2013; Mattila et al., 2017). However, due to the overall complexity, only a handful of research papers have managed to provide a *stability-guaranteed* NMB control design (Mattila et al., 2017). This situation is unsatisfactory because the control system stability is the primary requirement for all control systems and an unstable system is typically useless and potentially dangerous (Krstić et al., 1995; Slotine & Li, 1991).

The objective of this study is to design a *high-precision* and *stability-guaranteed* controller for multiple degrees-of-freedom ( $n$ -DOF) hydraulic robotic manipulators, while simultaneously substantially improving their *energy efficiency*. The solution suggests that: (1) A possibility for reducing hydraulic actuators' energy consumption can be realized by using servovalves in separate meter-in separate meter-out (SMISMO) control set-up (see Fig. 1(b)), enabling individual metering (pressure control) for the actuators' chambers. (2) A high-precision *piston motion*, *piston force* and *chamber pressure* tracking controller can be designed for the actuators in a  $n$ -DOF hydraulic robotic manipulator. The latter is designed by using the control design principles of the virtual decomposition control (VDC) approach (see Zhu, 2010; Zhu et al., 1997), allowing that the original complex system can be virtually decomposed to *modular* subsystems. This enables that the control design and its stability analysis can be performed locally at the subsystem level and, very importantly, the control system becomes modular in the sense that changing the control (or dynamics) of one subsystem does not affect the control equations of the rest of the system. A number of significant state-of-the-art control performance improvements have been reported with VDC for hydraulic robots (see Koivumäki & Mattila, 2015a,b, 2017a; Mattila et al., 2017; Zhu & Piedboeuf, 2005) and for electric robots (see Zhu et al., 1998; Zhu & De Schutter, 1999a,b, 2002; Zhu et al., 2013).

This paper provides the following contributions. (1) It is theoretically shown that hydraulic systems' energy consumption can be reduced using a SMISMO control setup. (2) Novel energy consumption optimizing chamber pressure trajectories are designed. (3) *Stability-guaranteed* high-precision SMISMO control for  $n$ -DOF hydraulic manipulators is proposed for the first time with experimental verifications in  $n$ -DOF. (4) It is shown that the triple objective of high-precision *piston position*, *piston force* and *chamber pressure* trackings can be design for hydraulic actuators. (5) The comparative experiments with a redundant 3-DOF hydraulic manipulator (having a payload of 475 kg) demonstrate that the proposed controller: (i) outperforms *all* non-VDC control methods (reviewed in Mattila et al., 2017) in motion control accuracy in view of a normalizing performance indicator  $\rho$ , and (ii) achieves an unprecedented piston motion and chamber pressure tracking accuracies in relation to the previous SMISMO-control methods. (6) In comparison

to state-of-the-art VDC controller with a conventional energy-inefficient servovalve control, *the actuators' total energy consumption is reduced by 45% without noticeable Cartesian position-tracking accuracy lost*.

Next, Section 2 is devoted to the SMISMO control; Section 2.1 reviews the SMISMO control strategies, Section 2.2 contributes to SMISMO control by theoretically showing its ability for the energy consumption reductions and, *very importantly*, Section 2.3 designs energy-optimized chamber pressure trajectories for the proposed control method. Section 3 introduces the VDC approach and designs the VDC-based SMISMO controller for the studied  $n$ -DOF hydraulic manipulator. Section 4 provides a rigorous stability proof for the overall control design. Section 5 demonstrates the control performance of the method in comparative experiments. Section 6 concludes the study.

## 2. SMISMO control

### 2.1. Previous works and their limitations

After SMISMO control was proposed in Jansson and Palmberg (1990), an intensive research have been performed for single-DOF hydraulic actuators. However, these single-DOF SMISMO actuator control designs are not immediately applicable to  $n$ -DOF systems and, thus, are not reviewed. An overview of different hardware layouts to realize SMISMO control can be found in Eriksson and Palmberg (2011). Today, e.g., digital flow control units in digital hydraulics (see Linjama, 2011) use an idea of individual metering.

An experimentally verified SMISMO control of  $n$ -DOF hydraulic manipulators was proposed for the first time by Mattila and Virvalo (2000). The control design for a two-DOF hydraulic manipulator was based on the computed torque control method using input/output linearization, and SMISMO control was realized with closed-loop proportional valves. Stability analysis and parameter uncertainties were not considered.

The SMISMO control of hydraulic manipulators has recently attracted significant interest in research; see Choi et al. (2015), Huova et al. (2010), Karvonen (2016), Liu et al. (2016), Lübbert et al. (2016) and Xu et al. (2015). Relying on relatively simple control implementations, the main interest in these studies is improving the energy efficiency of the system, while the system motion control performance is mainly neglected; only (Huova et al., 2010; Karvonen, 2016) showed some motion control data. In Choi et al. (2015) and Liu et al. (2016), only simulation results were presented. No stability analysis is provided in Choi et al. (2015), Huova et al. (2010), Karvonen (2016), Liu et al. (2016), Lübbert et al. (2016) and Xu et al. (2015).

Koivumäki and Mattila (2013) demonstrated early attempts to design a VDC-based controller for an SMISMO-controlled two-DOF hydraulic manipulator. The stability was proven (cursorily). Contrary to the present study, parameter uncertainties were neglected in Koivumäki and Mattila (2013). While reporting sufficiently improved motion control performance (not comparable to the present study; see Section 5.3), large chamber pressure tracking errors occurred during the driven test trajectories, limiting the applicability, e.g., in high-precision robotic applications.

The current state of the art in SMISMO control of hydraulic manipulators is shown in Liu and Yao (2008) and Lu and Yao (2014). Liu and Yao (2008) proposed a coordinated control of energy-saving programmable valves considering single-DOF boom dynamics (in fact, a three-DOF robotic arm, where only one of the joints was driven) and the hydraulic actuator dynamics. The two-level controller was designed on (backstepping based) adaptive robust control, guaranteeing closed-loop system stability and performance under various model uncertainties and disturbances. The advancement of the proposed method was demonstrated in experiments.

<sup>1</sup> In articulated systems, the associated multibody dynamics are nonlinear. Furthermore, hydraulic actuator dynamics can involve non-smooth and discontinuous nonlinearities due to actuator friction, hysteresis, control input saturation, or directional change of valve opening, and also many model and parameter uncertainties exist (Alleyne & Liu, 1999; Edge, 1997; Watton, 1989; Yao et al., 2001, 2014). Altogether, the complex dynamic behavior of hydraulic robotic systems (like manipulators) can be described by highly nonlinear coupled third-order differential equations.

<sup>2</sup> The aim is to design a specific feedforward term to proactively generate the required actuator forces from the required inverse motion dynamics (Mistry et al., 2010; Zhu, 2010).

Lu and Yao (2014) updated their previous controller in Liu and Yao (2008) by adding an accumulator to the system and improving the system energy consumption potential. A three-level stability-guaranteed adaptive robust controller was developed for the same single-DOF electro-hydraulic boom as in Liu and Yao (2008), and energy consumption reduction in relation to Liu and Yao (2008) was reported.

As discussed, stability-guaranteed NMB control methods can provide the most advanced control performance for hydraulic manipulators (Mattila et al., 2017). However, energy-efficient and high-precision NMB control for  $n$ -DOF hydraulic manipulators, with guaranteed control system stability, is still an open problem. *This problem is addressed in the present paper.* Furthermore, contrary to all the above reviewed studies, *the present study introduces a kinematic redundancy in its mechanical structure.*

## 2.2. Energy efficiency and SMISMO control

Currently, an electro-hydraulic (servo)valve control is a necessity for hydraulic actuators' high-precision control in terms of control accuracy and response time (Mattila et al., 2017).<sup>3</sup> Indeed, all state-of-the-art control methods for hydraulic robotic manipulators reviewed in Mattila et al. (2017) have employed a conventional servovalve control (see Fig. 1(a)). In this set-up, the valve meter-in (inlet) and meter-out (outlet) orifices are mechanically connected by a spool, making the system robust and easier to control (Eriksson & Palmberg, 2011).

The hydraulic cylinder piston force  $f_p$  can be written as

$$f_p = A_a p_a - A_b p_b \quad (1)$$

where  $A_a > A_b$  holds for the piston chamber areas, and  $p_a$  and  $p_b$  are the chamber pressures; see Fig. 1. In the conventional control, the piston force  $f_p$  is controllable, whereas the individual chamber pressures  $p_a$  and  $p_b$  are not. Thus, this type of system lacks flexibility, and meter-out orifices are needed to be dimensioned for an over-running load, leading to unnecessary losses in the orifices (Eriksson & Palmberg, 2011; Mattila & Virvalo, 2000).

In the SMISMO control (see Fig. 1(b)), the mechanical connection between the meter-in and meter-out orifices is removed, and each cylinder chamber is controlled with an individual (servo)valve. This makes the chamber pressures  $p_a$  and  $p_b$  controllable, and, in theory, a specific piston force  $f_p$  can be now obtained with an infinite number of chamber pressure combinations. *This enables a possibility for hydraulic actuators' energy consumption reductions*, if such high-precision chamber pressure trackings can be designed for  $p_a$  and  $p_b$  that the pressures can be set as low as practically possible. Obviously, this leads to a possibility to lower also the system supply pressure  $p_s$ .

Next, consider that both pistons in Fig. 1 are moving with velocity  $\dot{x} > 0$  to right with the maximum piston force  $f_{pmax} > 0$ . In this quadrant of  $\dot{x}$ - $f_p$  envelope, chamber A is the meter-in chamber and chamber B is the meter-out chamber. Then, the hydraulic energy consumption  $E_h$  can be written as

$$E_h = \int_0^t Q_a(\tau) p_s(\tau) d\tau = \int_0^t A_a \dot{x}(\tau) p_s(\tau) d\tau \quad (2)$$

<sup>3</sup> As an alternative to servovalve control, a displacement control (Grabbel & Ivantysynova, 2005; Hippalgaonkar & Ivantysynova, 2016) can be used for a hydraulic actuator control by regulating the variable displacement pump (VDP) fluid flow rate production, without using an energy dissipating control valve between the pump and the actuator. However, the dynamic response of VDPs is much slower compared with servovalves; response times for cutting-edge VDPs vary between 65–160 ms (Parker Hannifin, 2016, p. 6), whereas that of cutting-edge servovalves can be  $< 1.8$  ms (MOOG, 2015). Furthermore, the above mentioned displacement control studies lack of attention to high-bandwidth actuator tracking performance, which is essential for robotic purposes. However, some promising results are recently obtain in Hyon et al. (2017b) with a hydraulic hybrid servo booster.

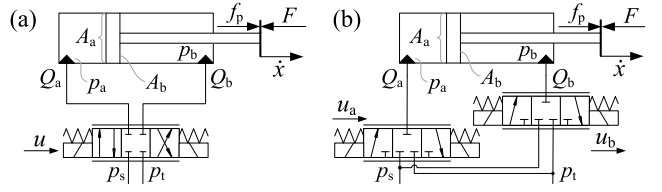


Fig. 1. (a) shows a conventional control set-up for an asymmetric cylinder. (b) shows a SMISMO control set-up for an asymmetric cylinder.

where  $Q_a$  is the fluid flow rate to chamber A. Regulating  $E_h$  with  $Q_a (= A_a \dot{x})$  is generally irrelevant; a slower velocity  $\dot{x}$  increases a task completion time  $t$  in (2), thus, providing very minor (if any) reductions in the energy consumption. Consequently, the remaining option for energy efficiency is to regulate the system supply pressure  $p_s$  (by lowering  $p_a$  and  $p_b$ ).

In the analyzed quadrant ( $\dot{x} > 0$ ,  $f_{pmax} > 0$ ), the needed supply pressure in the conventional control can be written as (Johnson, 1995)

$$p_{s(CC)} = \frac{3 f_{pmax}}{2 A_a} \quad (3)$$

The SMISMO control can provide a possibility for energy consumption reductions due to its ability for the individual chamber pressure control. Let the chamber pressures be minimized by designing a constant pressure margin  $\Delta p_c$  (typically 5–20 bar) across both of the meter-in and meter-out orifices. Then, in the analyzed quadrant, the needed supply pressure in the SMISMO control can be written as

$$p_{s(SMISMO)} = p_a + \Delta p_c = \frac{f_{pmax} + (A_a + A_b) \Delta p_c}{A_a} \quad (4)$$

using (1) and  $p_b = p_t + \Delta p_c$ , where  $p_t = 0$  is the return line pressure. Then, Condition 1 can be derived from (3) and (4).

**Condition 1.** If  $\Delta p_c < \frac{f_{pmax}}{2(A_a + A_b)}$ , then  $p_{s(SMISMO)} < p_{s(CC)}$ .

It follows directly from (2) that reduced energy consumption can be obtained with the SMISMO control, when Condition 1 holds. As an example, let  $f_{pmax} = 100$  kN,  $A_a = 5.02 \times 10^{-3}$  m<sup>2</sup> and  $A_b = 3.44 \times 10^{-3}$  m<sup>2</sup> (dimensions of cylinder 1 in the studied manipulator). Then, for the energy consumption reductions,  $\Delta p_c < 59$  bar should be selected.

**Remark 1.** Respective analysis to Condition 1 can shown to be valid in all four quadrants of  $\dot{x}$ - $f_p$  envelope. If a constant pressure pump is used, Condition 1 can be used to set the system constant supply pressure level. For further energy consumption reductions, the system supply pressure  $p_s(t)$  needs to be controlled such that  $p_s(t) = p_{in}(t) + \Delta p_c$ ,  $\forall t$ , where  $p_{in}(t)$  is the meter-in chamber pressure. Methods for advanced supply pressure control can be found in Koivumäki and Mattila (2017b), Lovrec and Ulaga (2007) and Mattila et al. (2017).

The remaining question is: *How to design such a high-precision chamber pressure tracking control that  $p_a$  and  $p_b$  can be minimized according to  $\Delta p_c$ , while simultaneously designing a high-precision piston motion tracking?* This is not a simple task. It is well known that designing a high-precision motion and force tracking controller for the conventionally controlled actuator (see Fig. 1(a)) is a challenging task due to the system significant nonlinearities (Alleyne & Liu, 1999; Edge, 1997; Watton, 1989; Yao et al., 2001, 2014). In the SMISMO control (see Fig. 1(b)), the control design task becomes even more complicated (Eriksson & Palmberg, 2011). Thus, designing both high-precision piston motion and chamber pressure trackings in the SMISMO-control is an extreme control design challenge for a single actuator alone. Evidently, this task becomes even more multifaceted challenge, when  $n$ -DOF manipulator's nonlinear dynamics are needed to be considered. *This problem is addressed in the present paper.*

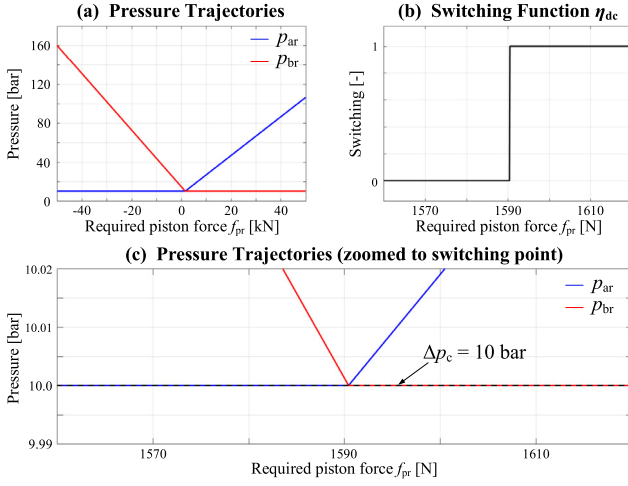


Fig. 2. Non-differentiable chamber pressure trajectories. (For interpretation of colors in this figure, the reader is referred to the web version of this article.)

### 2.3. Energy consumption optimizing SMISMO trajectories

Let the required piston force  $f_{pr}(t)$  (a control design variable specified in Section 3.4) be known and a smooth (differentiable) function. Then, the following design constraints are imposed for required chamber pressure trajectories  $p_{ar}(t)$  and  $p_{br}(t)$ :

**Condition 2.** In view of (1), the following constraint must hold for the chamber pressure trajectories  $p_{ar}$  and  $p_{br}$ :

$$f_{pr} = A_a p_{ar} - A_b p_{br}. \quad (5)$$

**Condition 3.** To avoid cavitation in the chambers,  $p_{ar}(t) \geq \Delta p_c$  and  $p_{br}(t) \geq \Delta p_c$  must hold  $\forall t$ , where  $\Delta p_c > 0$  is a constant pressure margin, but also sets a desired minimum pressure level for the cylinder chambers.

**Condition 4.** To minimize the chamber pressure levels,  $\Delta p_c$  must hold at least one of the chamber pressure trajectories  $\forall t$ , i.e.,  $\min\{p_{ar}(t), p_{br}(t)\} = \Delta p_c, \forall t$ .

In view of Conditions 2–4, the following chamber pressure trajectories are designed for  $p_{ar}$  and  $p_{br}$  using the known  $f_{pr}(t)$ :

$$p_{ar}(f_{pr}) = \frac{f_{pr} + A_b \Delta p_c}{A_a} \eta_{dc}(f_{pr}) + \Delta p_c [1 - \eta_{dc}(f_{pr})] \quad (6)$$

$$p_{br}(f_{pr}) = -\frac{f_{pr} - A_a p_{ar}(f_{pr})}{A_b} \quad (7)$$

where a discontinuous (non-differentiable) switching function  $\eta_{dc}(f_{pr})$  is designed as

$$\eta_{dc}(f_{pr}) = \begin{cases} 1, & \text{if } f_{pr} - \Delta p_c(A_a - A_b) \geq 0 \\ 0, & \text{otherwise} \end{cases} \quad (8)$$

Fig. 2(a) shows the behavior of the designed chamber pressure trajectories (6) and (7) as a function of  $f_{pr}$ . In the figure,  $\Delta p_c = 10$  bar,  $A_a = 5.02 \times 10^{-3} \text{ m}^2$  and  $A_b = 3.44 \times 10^{-3} \text{ m}^2$  are used. Fig. 2(b) shows the behavior of the discontinuous switching function  $\eta_{dc}(f_{pr})$  in (8), which defines a switching point where both  $p_{ar}$  and  $p_{br}$  equal to  $\Delta p_c$ . Fig. 2(c) shows a zoomed view to the switching point. The validity of Condition 2 can be shown by substituting (6) and (7) into (5). The validity of Conditions 3 and 4 can be seen in Fig. 2.

If time derivatives  $\dot{p}_{ar}$  and  $\dot{p}_{br}$  are needed in the control design, the designed pressure trajectories in (6) and (7) cannot be used due to the discontinuous (non-differentiable) switching function  $\eta_{dc}(f_{pr})$ . Thus,

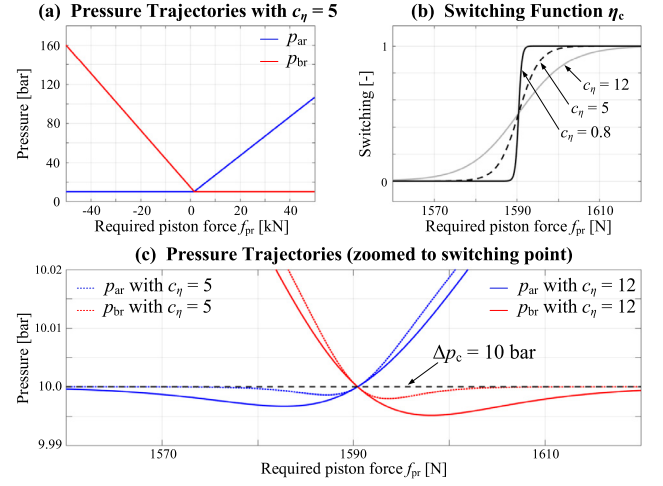


Fig. 3. Continuously differentiable chamber pressure trajectories. (For interpretation of colors in this figure, the reader is referred to the web version of this article.)

the following smooth (continuously differentiable) switching function  $\eta_c(f_{pr})$  is designed

$$\eta_c(f_{pr}) = \frac{\tanh([f_{pr} - \Delta p_c(A_a - A_b)]/c_\eta) + 1}{2} \quad (9)$$

where  $c_\eta > 0$  is a sufficiently small constant. Now, the differentiable chamber pressure trajectories can be designed as

$$p_{ar}(f_{pr}) = \frac{f_{pr} + A_b \Delta p_c}{A_a} \eta_c(f_{pr}) + \Delta p_c [1 - \eta_c(f_{pr})] \quad (10)$$

$$p_{br}(f_{pr}) = -\frac{f_{pr} - A_a p_{ar}(f_{pr})}{A_b} \quad (11)$$

provided that  $\dot{f}_{pr}$  exists.

Fig. 3(a) shows the behavior of the designed smooth chamber pressure trajectories in (10) and (11); note the similarity to Fig. 2(a). Fig. 3(b) shows the behavior of the smooth switching function  $\eta_c(f_{pr})$  in (9) with three  $c_\eta$  values. The smaller the  $c_\eta$ , the faster the switching rate of  $\eta_c(f_{pr})$ , and when  $c_\eta \rightarrow 0$ , then  $\eta_c(f_{pr}) \rightarrow \eta_{dc}(f_{pr})$ . Fig. 3(c) shows a zoomed view to the switching point with  $c_\eta = 5$  and  $c_\eta = 12$ . Some undershoot exists in  $p_{ar}$  and  $p_{br}$  in relation to  $\Delta p_c$ , making Conditions 3 and 4 invalid in the neighborhood of the switching point, however, the amount of overshoot can be adjusted to be minimal with  $c_\eta$ . Very importantly,  $p_{ar}$  and  $p_{br}$  in (10) and (11) are constrained by  $f_{pr}(t)$  in (5), i.e., Condition 2 holds; this can be shown by substituting (10) and (11) into (5). Finally, note that the switching point for the pressure trajectories in (10) and (11) is automatically adjusted with  $\Delta p_c$ . Thus,  $c_\eta$  and  $\Delta p_c$  are the parameters governing the pressure trajectory behaviors in (10) and (11).

### 3. Virtual decomposition control

In this study, the control system is designed based on a novel VDC approach; see Zhu et al. (1997) and Zhu (2010). VDC is the first rigorous control method to take full advantage of Newton–Euler dynamics, and its unique *subsystem-dynamics-based control* design philosophy has brought a *modularity* to control system engineering, enabling, e.g., that changing the control (or dynamics) of one subsystem does not affect the control equations of the rest of the system. As will be shown, an adaptive control can be incorporated into the control design to cope with all uncertain parameters involved in the subsystems' dynamics.

In VDC, the original system is *virtually decomposed* into modular subsystems (*objects and open chains*), allowing that the control design and stability analysis can be performed at the subsystem level without imposing additional approximations. The virtual decomposition is



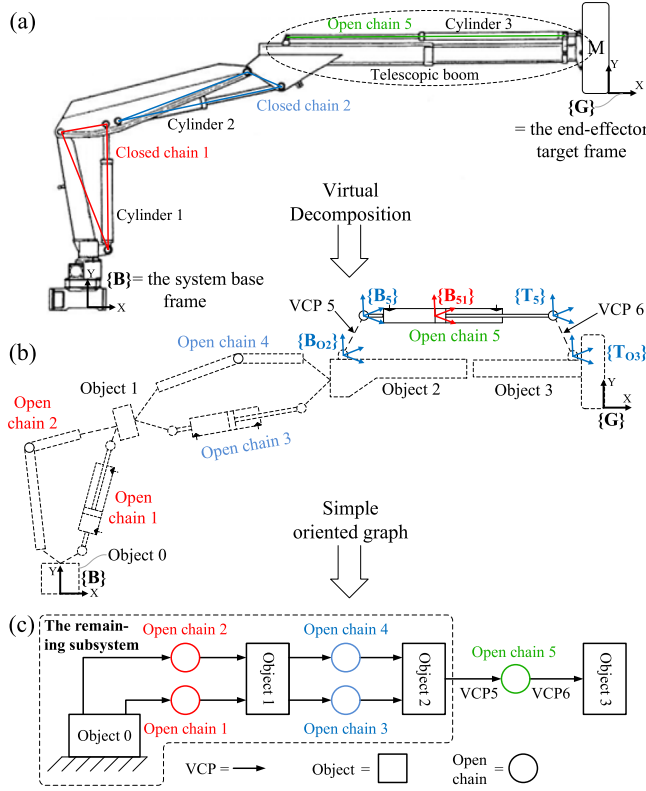


Fig. 4. (a) The studied robotic manipulator. (b) The virtual decomposition of the system. (c) The simple oriented graph of the system. (For interpretation of colors in this figure, the reader is referred to the web version of this article.)

performed by placing conceptual *virtual cutting points* (VCPs), which are directed separation interfaces that conceptually cut through a rigid body. At a VCP, two parts resulting from the virtual cut maintain equal positions and orientations. Thus, the VCP forms a virtual cutting surface on which six-dimensional force/moment vectors (see Appendix A) can be exerted from one part to another. It is simultaneously interpreted as a *driving* VCP by one subsystem (from which the force/moment vector is exerted) and as a *driven* VCP by another subsystem (to which the force/moment vector is exerted) (Zhu, 2010).

Fig. 4(a) shows the studied 3-DOF hydraulic manipulator. The system has two hydraulic cylinder actuated rotational joints (closed-chain structures in red and blue), and a hydraulic cylinder actuated prismatic joint (in green) for a telescopic boom. The telescopic boom makes the system redundant. Although a 3-DOF system is studied, the approach developed in this paper is easily extendable for systems with any number of actuators.

Fig. 4(b) shows the virtual decomposition of the system. Note that the closed-chain structures (in Fig. 4(a)) are decomposed to open chains; *unactuated revolute* open chains 2 and 4, and *actuated prismatic* open chains 1 and 3. By neglecting the friction between the bearing-mounted sliding booms, the telescopic boom can be decomposed to objects 2 and 3, and an *actuated prismatic* open chain 5 (in green). This treatment enables that: (1) the control design for cylinder 3 becomes independent from the sliding booms, and (2) the control design for all actuated open chains becomes modular at the subsystem level. Similar modularity is obtained for the objects 0–3, and for the unactuated open chains 2 and 4. Fixed body frames are attached to the system to describe the motion and force specifications (for simplicity, only the frames involved to cylinder 3 are shown in Fig. 4(b)). Blue frames are frames at the VCPs and red frames are frames at the subsidiary VCPs of the open chain.

After the virtual decomposition, the system is represented by a simple oriented graph (SOG), which is shown in Fig. 4(c). The SOG describes

the system's topological structure and the dynamic relationships among the decomposed subsystems. In the SOG, each subsystem represents a *node*, and each VCP represents a *directed edge*, the direction of which defines the force reference direction. Nodes that have pointing-away edges only are called *source nodes*, and nodes that have pointing-to edges only are called *sink nodes*. No loop is allowed in a SOG (Zhu, 2010).

As mentioned, VDC allows that changing the control (or dynamics) of a subsystem *does not affect the control equations of the rest of the system*. Furthermore, when all subsystems qualify as *virtually stable* (see Definition 3 in Appendix C),  $L_2$  and  $L_\infty$  stability (see Lemma 1 in Appendix B) of the entire system can be guaranteed. Thus, the *main objectives in this study are to*

- (1) design a high-precision *motion, force and pressure* tracking control for the SMISMO-controlled hydraulic actuators, using the pressure trajectories in (10) and (11), and
- (2) design a *virtually stable* structure for the above mentioned controller to ensure its direct connectivity to the previously designed VDC-based controllers for  $n$ -DOF hydraulic manipulators in Koivumäki and Mattila (2015a,b, 2017a).

For the above, hydraulic cylinder 3 (composing of open chain 5 dynamics and the actuator fluid dynamics) in Fig. 5 is used as an illustrative example. The virtually stable control designs for the remaining subsystems (delimited with the dashed line in Fig. 4(c)) and for object 3 can be obtained as shown in Remark 2.

**Remark 2.** The control design for cylinders 1 and 2 can be obtained by following a procedure similar to that presented for cylinder 3. The control design for the unactuated open chains (open chains 2 and 4 in Fig. 4), and kinematic and dynamic relations in the system closed chains can be found in details in Koivumäki and Mattila (2015a,b). The control design for the objects is a trivial case and can be obtained as described, e.g., in Koivumäki and Mattila (2015a) and Zhu (2010).

Next, the kinematics and dynamics (open chain 5 dynamics and cylinder 3 dynamics) for the SMISMO controlled hydraulic actuator assembly are specified in Sections 3.1 and 3.2. Then, the detailed control laws for the proposed SMISMO controller are derived in Sections 3.3 and 3.4, where the *control design procedure is clarified in the remarks*. The system stability analysis is provided later in Section 4.

### 3.1. Open chain 5: Kinematics and dynamics

The notation in this section follows a standard notation used in VDC. For more details on the linear/angular velocity vectors  ${}^A V \in \mathbb{R}^6$ , the force/moment vectors  ${}^A F \in \mathbb{R}^6$  and the transformation matrices  ${}^A U_B \in \mathbb{R}^{6 \times 6}$ , see Appendix A.

Open chain 5 (composing of rigid links 5 and 51) is shown in Fig. 5. For the attached frames at VCP 5 and VCP 6, denoted in blue in Figs. 4(b) and 5, the following relations hold:

$$\{T_{O3}\} = \{T_5\} \quad (12)$$

$$\{B_{O2}\} = \{B_5\}. \quad (13)$$

The kinematics of subsystems can be computed by propagating along the direction of the VCP flow in the SOG (see Fig. 4) from the source node (object 0) toward the sink node (object 3). Then, given  ${}^{B_{O2}} V \in \mathbb{R}^6$ , the linear/angular velocity vector  ${}^{B_5} V$  at the driven VCP of open chain 5 can be written as

$${}^{B_5} V = {}^{B_{O2}} V \quad (14)$$

in view of (13). Then, the remaining linear/angular velocity vectors in open chain 5 can be written as

$${}^{B_{51}} V = {}^{B_5} V + {}^{B_5} U_{B_{51}}^T {}^{B_5} V \quad (15)$$

$${}^{T_5} V = {}^{B_{51}} U_{T_5}^T {}^{B_{51}} V \quad (16)$$

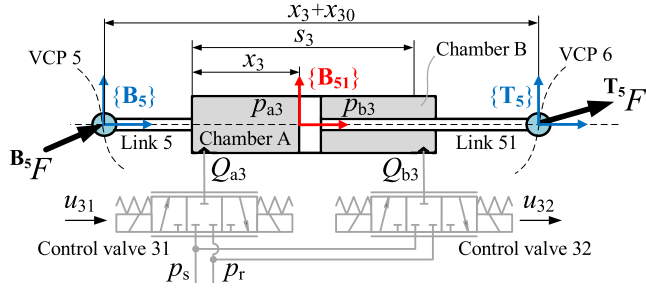


Fig. 5. The hydraulic actuator assembly (cylinder 3), composing of the prismatic open chain 5 (with the black line), and the fluid dynamics with the SMISMO control layout (in gray). (For interpretation of colors in this figure, the reader is referred to the web version of this article.)

where  $\mathbf{x}_f = [1 \ 0 \ 0 \ 0 \ 0 \ 0]^T$  and  $\dot{x}_3$  is the piston velocity of cylinder 3. Then, in view of (12), the linear/angular velocity vector  $\mathbf{T}_{03}V \in \mathbb{R}^6$  at the driven VCP of object 3 can be written as

$$\mathbf{T}_{03}V = \mathbf{T}_5V. \quad (17)$$

After the kinematics, the dynamics of subsystems can be computed by propagating along the opposite direction of the SOG from the sink node toward the source node (see Fig. 4). First, using (A.5) in Appendix A, the dynamics of link 5 (the cylinder case) and link 51 (the cylinder piston) can be written as

$$\mathbf{M}_{B_5} \frac{d}{dt}(\mathbf{B}_5V) + \mathbf{C}_{B_5}(\mathbf{B}_5\omega)\mathbf{B}_5V + \mathbf{G}_{B_5} = \mathbf{B}_5F^* \quad (18)$$

$$\mathbf{M}_{B_{51}} \frac{d}{dt}(\mathbf{B}_{51}V) + \mathbf{C}_{B_{51}}(\mathbf{B}_{51}\omega)\mathbf{B}_{51}V + \mathbf{G}_{B_{51}} = \mathbf{B}_{51}F^* \quad (19)$$

where  $\mathbf{M}_{B_5}, \mathbf{M}_{B_{51}} \in \mathbb{R}^{6 \times 6}$  are the mass matrices,  $\mathbf{C}_{B_5}(\mathbf{B}_5\omega), \mathbf{C}_{B_{51}}(\mathbf{B}_{51}\omega) \in \mathbb{R}^{6 \times 6}$  are the Coriolis and centrifugal matrices, and  $\mathbf{G}_{B_5}, \mathbf{G}_{B_{51}} \in \mathbb{R}^6$  are the gravity vectors; see Appendix A.

Given  $\mathbf{T}_{03}F \in \mathbb{R}^6$ , the force/moment vector in  $\mathbf{T}_5F$  at the driving VCP of open chain 5 can be obtained in view of (12) as

$$\mathbf{T}_5F = \mathbf{T}_{03}F. \quad (20)$$

Then, the remaining force/moment vectors can be obtained as

$$\mathbf{B}_{51}F = \mathbf{B}_{51}F^* + \mathbf{B}_{51}\mathbf{U}_{T_5}^T \mathbf{T}_5F \quad (21)$$

$$\mathbf{B}_5F = \mathbf{B}_5F^* + \mathbf{B}_5\mathbf{U}_{B_{51}}^T \mathbf{B}_{51}F. \quad (22)$$

The force/moment vector  $\mathbf{B}_{02}F \in \mathbb{R}^6$  at the driving VCP of object 2 can be obtained from (22) as

$$\mathbf{B}_{02}F = \mathbf{B}_5F. \quad (23)$$

Finally, cylinder 3 piston force can be written as

$$f_{c3} = \mathbf{x}_f^T \mathbf{B}_{51}F. \quad (24)$$

### 3.2. Dynamics of the hydraulic actuator

It is well known that the cylinder piston friction is a highly nonlinear and hard-to-model phenomenon. This can make a considerable difference between the cylinder pressure-induced force  $f_p$  and the cylinder output force  $f_c$ . Taking the friction into account, the piston force  $f_{p3}$  for cylinder 3 can be written as

$$f_{p3} = f_{c3} + f_{f3} \quad (25)$$

where  $f_{c3}$  comes from (24), and  $f_{f3}$  is the friction force. In this study, a dynamics friction model from Zhu and Piedboeuf (2005) is used. The friction model considers the Coulomb friction, Stribeck friction, viscous friction, the average deformation of the seal bristles, and provides a smooth transition between presliding and sliding motion. Very importantly, the model is differentiable (for smooth friction dynamics),

and it can be written in a parametrized form for an adaptive friction compensation as

$$f_{f3} = \mathbf{Y}_{f3}\boldsymbol{\theta}_{f3} \quad (26)$$

where  $\mathbf{Y}_{f3} \in \mathbb{R}^{1 \times 7}$  and  $\boldsymbol{\theta}_{f3} \in \mathbb{R}^7$  are defined in Zhu and Piedboeuf (2005) in details. Additionally, some other friction model with fewer adaptable friction parameters, e.g., Zhu (2014) or Yao et al. (2015), can be used for the friction compensation.

In addition to (25),  $f_{p3}$  can be written as

$$f_{p3} = A_{a3}p_{a3} - A_{b3}p_{b3} \quad (27)$$

where  $A_{a3} > A_{b3}$  holds for the piston areas, and  $p_{a3}$  and  $p_{b3}$  are the chamber pressures; see Fig. 5.

The following two assumptions are made.

**Assumption 1.** The cylinder piston position  $x_3$  never reaches its two ends, i.e.,  $x_3 > 0$  and  $s_3 - x_3 > 0$ , where  $s_3$  is the piston maximum stroke.

**Assumption 2.** The following system pressure relations hold:  $p_s > p_{a3} > p_r \geq 0$  and  $p_s > p_{b3} > p_r \geq 0$ , where  $p_s$  and  $p_r$  are the system supply and return line pressures.

Similarly to Koivumäki and Mattila (2015b), Liu and Yao (2008), Lu and Yao (2014), Mattila and Virvalo (2000) and Zhu and Piedboeuf (2005), if high-bandwidth (servo) valves are used, it is reasonable to neglect the control valve dynamics. Then, the fluid flow rates  $Q_{a3}$  and  $Q_{b3}$  entering cylinder 3 chamber A and chamber B can be written as

$$Q_{a3} = c_{p1}v(p_s - p_{a3})S(u_{31})u_{31} + c_{n1}v(p_{a3} - p_r)S(-u_{31})u_{31} \quad (28)$$

$$Q_{b3} = c_{p2}v(p_s - p_{b3})S(u_{32})u_{32} + c_{n2}v(p_{b3} - p_r)S(-u_{32})u_{32} \quad (29)$$

where  $c_{p1} > 0$  and  $c_{n1} > 0$  are the flow coefficients of the chamber A control valve,  $u_{31}$  is the control valve voltage,  $c_{p2} > 0$  and  $c_{n2} > 0$  are the flow coefficients of the chamber B control valve,  $u_{32}$  is the control valve voltage, and the pressure-related function  $v(\cdot)$  and the selective function  $S(u)$  are defined as

$$v(\cdot) = \text{sign}(\cdot)\sqrt{|\cdot|} \quad (30)$$

$$S(u) = \begin{cases} 1, & \text{if } u > 0 \\ 0, & \text{if } u \leq 0. \end{cases} \quad (31)$$

Similarly to, e.g., Koivumäki and Mattila (2015b), Liu and Yao (2008) and Lu and Yao (2014), the actuator internal leakages are neglected; usually, these are minimal (if any) with well-sealed hydraulic cylinders. Then, using (28) and (29), the fluid continuity equations in the cylinder chambers can be written as

$$\dot{p}_{a3} = \frac{\beta_f}{A_{a3}x_3} (Q_{a3} - A_{a3}\dot{x}_3) = \frac{\beta_f}{A_{a3}} \left( u_{v31} - \frac{A_{a3}\dot{x}_3}{x_3} \right) \quad (32)$$

$$\dot{p}_{b3} = \frac{\beta_f}{A_{b3}(s_3 - x_3)} (Q_{b3} + A_{b3}\dot{x}_3) = \frac{\beta_f}{A_{b3}} \left( u_{v32} + \frac{A_{b3}\dot{x}_3}{s_3 - x_3} \right) \quad (33)$$

where  $\beta_f$  is the bulk modulus of the fluid. The valve voltage-related terms  $u_{v31}$  and  $u_{v32}$  in (32) and (33) can be written as

$$\begin{aligned} u_{v31} &= \frac{c_{p1}v(p_s - p_{a3})}{x_3} S(u_{31})u_{31} + \frac{c_{n1}v(p_{a3} - p_r)}{x_3} S(-u_{31})u_{31} \\ &= -\mathbf{Y}_{v31}\boldsymbol{\theta}_{v31} \end{aligned} \quad (34)$$

$$\begin{aligned} u_{v32} &= \frac{c_{p2}v(p_s - p_{b3})}{s_3 - x_3} S(u_{32})u_{32} + \frac{c_{n2}v(p_{b3} - p_r)}{s_3 - x_3} S(-u_{32})u_{32} \\ &= -\mathbf{Y}_{v32}\boldsymbol{\theta}_{v32}. \end{aligned} \quad (35)$$

where the regressor vectors  $\mathbf{Y}_{v31}, \mathbf{Y}_{v32} \in \mathbb{R}^{1 \times 2}$  and the parameter vectors  $\boldsymbol{\theta}_{v31}, \boldsymbol{\theta}_{v32} \in \mathbb{R}^2$  are given in Appendix E.

Finally, in view of Assumptions 1 and 2, univalences between  $u_{31}$  and  $u_{v31}$  and between  $u_{32}$  and  $u_{v32}$  exist.<sup>4</sup> Thus, for the given  $u_{v31}$  and

<sup>4</sup> When Assumptions 1 and 2 hold,  $x_3 > 0$ ,  $s_3 - x_3 > 0$ ,  $v(p_s - p_{a3}) > 0$ ,  $v(p_{a3} - p_r) > 0$ ,  $v(p_s - p_{b3}) > 0$ , and  $v(p_{b3} - p_r) > 0$  hold. Thus, non-singular solutions for (34)–(37) are ensured.

$u_{v32}$ , the unique valve control voltages  $u_{31}$  and  $u_{32}$  can be found as

$$u_{31} = \frac{x_3 S(u_{v31})}{c_{p1} v(p_s - p_{a3})} u_{v31} + \frac{x_3 S(-u_{v31})}{c_{n1} v(p_{a3} - p_r)} u_{v31} \quad (36)$$

$$u_{32} = \frac{(s_3 - x_3) S(u_{v32})}{c_{p2} v(p_s - p_{b3})} u_{v32} + \frac{(s_3 - x_3) S(-u_{v32})}{c_{n2} v(p_{b3} - p_r)} u_{v32}. \quad (37)$$

### 3.3. Open chain 5: Control

In VDC, the required velocity serves as a reference trajectory for system. The control objective is to make the controlled velocities track the required velocities. The general format of the required velocity includes the desired velocity and one or more terms that are related to control errors (Zhu, 2010). The required cylinder velocity  $\dot{x}_{ir}$  for the  $i$ th actuator,  $\forall i \in \{1, 2, 3\}$ , is designed as

$$\dot{x}_{ir} = \dot{x}_{id} + \lambda_{xi} (x_{id} - x_i) \quad (38)$$

where  $x_{id}$  is the desired piston position, and  $\lambda_{xi} > 0$  is the position control gain. In the Cartesian space control, the desired Cartesian motion data can be converted to the respective desired actuator space values  $\dot{x}_{id}$  and  $x_{id}$ , as shown in Koivumäki and Mattila (2015a).

Let  $\mathbf{B}_{02} V_r \in \mathbb{R}^6$  be known. Using (14)–(17), the required linear/angular velocity vectors in open chain 5 can be written as

$$\mathbf{B}_5 V_r = \mathbf{B}_{02} V_r \quad (39)$$

$$\mathbf{B}_{51} V_r = \mathbf{x}_f \dot{x}_{3r} + \mathbf{B}_5 \mathbf{U}_{\mathbf{B}_{51}}^T \mathbf{B}_5 V_r \quad (40)$$

$$\mathbf{T}_5 V_r = \mathbf{B}_{51} \mathbf{U}_{\mathbf{T}_5}^T \mathbf{B}_{51} V_r \quad (41)$$

$$\mathbf{T}_{03} V_r = \mathbf{T}_5 V_r. \quad (42)$$

Then, using (14), (15), (39) and (40), the required net force/moment vectors for link 5 (the cylinder case) and link 51 (the cylinder piston) can be written as

$$\mathbf{B}_5 F_r^* = \mathbf{Y}_{\mathbf{B}_5} \hat{\boldsymbol{\theta}}_{\mathbf{B}_5} + \mathbf{K}_{\mathbf{B}_5} (\mathbf{B}_5 V_r - \mathbf{B}_5 V) \quad (43)$$

$$\mathbf{B}_{51} F_r^* = \mathbf{Y}_{\mathbf{B}_{51}} \hat{\boldsymbol{\theta}}_{\mathbf{B}_{51}} + \mathbf{K}_{\mathbf{B}_{51}} (\mathbf{B}_{51} V_r - \mathbf{B}_{51} V) \quad (44)$$

where, by substituting  $\mathbf{A}$  for  $\mathbf{B}_5$  and  $\mathbf{B}_{51}$ ,  $\mathbf{Y}_{\mathbf{A}} \boldsymbol{\theta}_{\mathbf{A}} \in \mathbb{R}^6$  is the model-based feedforward compensation term (see Appendix A) for the rigid body dynamics in (18) and (19);  $\hat{\boldsymbol{\theta}}_{\mathbf{A}}$  is the estimate of the parameter vector  $\boldsymbol{\theta}_{\mathbf{A}} \in \mathbb{R}^{13}$ ; and  $\mathbf{K}_{\mathbf{A}} \in \mathbb{R}^{6 \times 6}$  is a positive-definite gain matrix for the velocity feedback control.

The estimated parameter vectors  $\hat{\boldsymbol{\theta}}_{\mathbf{B}_{51}}$  and  $\hat{\boldsymbol{\theta}}_{\mathbf{B}_5}$ , in (43) and (44), need to be updated. Define

$$\mathbf{s}_{\mathbf{B}_{51}} = \mathbf{Y}_{\mathbf{B}_{51}}^T (\mathbf{B}_{51} V_r - \mathbf{B}_{51} V) \quad (45)$$

$$\mathbf{s}_{\mathbf{B}_5} = \mathbf{Y}_{\mathbf{B}_5}^T (\mathbf{B}_5 V_r - \mathbf{B}_5 V). \quad (46)$$

Then, using the  $\mathcal{P}$  function in Appendix D, the  $\gamma$ th elements of  $\hat{\boldsymbol{\theta}}_{\mathbf{B}_{51}}$  and  $\hat{\boldsymbol{\theta}}_{\mathbf{B}_5}$  are updated,  $\forall \gamma \in \{1, 2, \dots, 13\}$ , as

$$\hat{\theta}_{\mathbf{B}_{51}\gamma} = \mathcal{P}(\mathbf{s}_{\mathbf{B}_{51}\gamma}, \rho_{\mathbf{B}_{51}\gamma}, \underline{\theta}_{\mathbf{B}_{51}\gamma}, \bar{\theta}_{\mathbf{B}_{51}\gamma}, t) \quad (47)$$

$$\hat{\theta}_{\mathbf{B}_5\gamma} = \mathcal{P}(\mathbf{s}_{\mathbf{B}_5\gamma}, \rho_{\mathbf{B}_5\gamma}, \underline{\theta}_{\mathbf{B}_5\gamma}, \bar{\theta}_{\mathbf{B}_5\gamma}, t) \quad (48)$$

where, by substituting  $\mathbf{A}$  for  $\mathbf{B}_5$  and  $\mathbf{B}_{51}$ ,  $\hat{\theta}_{\mathbf{A}\gamma}$  is the  $\gamma$ th element of  $\hat{\boldsymbol{\theta}}_{\mathbf{A}}$ ;  $\mathbf{s}_{\mathbf{A}\gamma}$  is the  $\gamma$ th element of  $\mathbf{s}_{\mathbf{A}}$ ;  $\rho_{\mathbf{A}\gamma} > 0$  is the update gain;  $\underline{\theta}_{\mathbf{A}\gamma}$  is the lower bound of  $\theta_{\mathbf{A}\gamma}$ ;  $\bar{\theta}_{\mathbf{A}\gamma}$  is the upper bound of  $\theta_{\mathbf{A}\gamma}$ .

The required force/moment vectors in open chain 5 can be obtained by reusing (20)–(23) as

$$\mathbf{T}_5 F_r = \mathbf{T}_{03} F_r \quad (49)$$

$$\mathbf{B}_{51} F_r = \mathbf{B}_{51} F_r^* + \mathbf{B}_{51} \mathbf{U}_{\mathbf{T}_5}^T \mathbf{T}_5 F_r \quad (50)$$

$$\mathbf{B}_5 F_r = \mathbf{B}_5 F_r^* + \mathbf{B}_5 \mathbf{U}_{\mathbf{B}_{51}}^T \mathbf{B}_{51} F_r \quad (51)$$

$$\mathbf{B}_{02} F_r = \mathbf{B}_5 F_r. \quad (52)$$

The required actuation force of cylinder 3 can be written as

$$f_{c3r} = \mathbf{x}_f^T \mathbf{B}_{51} F_r. \quad (53)$$

**Remark 3.** Subject open chain 5 control, a *stability-preventing term* ( $f_{c3r} - f_{c3}(\dot{x}_{3r} - \dot{x}_3)$ ) will appear in the time derivative  $\dot{v}_{oc5}$  of the non-negative accompanying function  $v_{oc5}$ ; see (F.2) in Lemma 4 in Appendix F. Next, in Section 3.4, a *stabilizing counterpart* is designed for the *stability-preventing term*.

### 3.4. Control of the hydraulic actuator

In view of (25) and (26), the following control law is designed for cylinder 3

$$f_{p3r} = f_{c3r} + \mathbf{Y}_{f3} \hat{\boldsymbol{\theta}}_{f3}. \quad (54)$$

The estimated friction parameter vector  $\hat{\boldsymbol{\theta}}_{f3}$  needs to be updated. Define

$$\mathbf{s}_{f3} = (\dot{x}_{3r} - \dot{x}_3) \mathbf{Y}_{f3}^T. \quad (55)$$

Then, the  $\gamma$ th element of  $\hat{\boldsymbol{\theta}}_{f3}$  is updated, using the  $\mathcal{P}$  function in Appendix D, as

$$\hat{\theta}_{f3\gamma} = \mathcal{P}(\mathbf{s}_{f3\gamma}, \rho_{f3\gamma}, \underline{\theta}_{f3\gamma}, \bar{\theta}_{f3\gamma}, t), \quad \forall \gamma \in \{1, 2, \dots, 7\} \quad (56)$$

where  $\hat{\theta}_{f3\gamma}$  is the  $\gamma$ th element of  $\hat{\boldsymbol{\theta}}_{f3}$ ;  $\mathbf{s}_{f3\gamma}$  is the  $\gamma$ th element of  $\mathbf{s}_{f3}$ ;  $\rho_{f3\gamma} > 0$  is the update gain;  $\underline{\theta}_{f3\gamma}$  is the lower bound of  $\theta_{f3\gamma}$ ; and  $\bar{\theta}_{f3\gamma}$  is the upper bound of  $\theta_{f3\gamma}$ .

Next, let the desired position  $x_{id}$  in (38) be a continuously differentiable function in  $C^2$ , i.e.,  $\{x_{id}, \dot{x}_{id}, \ddot{x}_{id}, x_{id}^{(3)}\} \in L_\infty$  holds. Then, similarly to Zhu (2010) and Zhu and Piedboeuf (2005), it can be seen from (38)–(54) that  $f_{p3r}$  in (54) is a smooth function, i.e.,  $\dot{f}_{p3r}(t)$  exists  $\forall t$ . The existence of  $\dot{f}_{p3r}$  is needed next in sections *Control of Chamber A* and *Control of Chamber B* as the time derivatives of the chamber pressure trajectories  $p_{ar}(f_{pr})$  in (10) and  $p_{br}(f_{pr})$  in (11) are needed in the control design.

#### Control of chamber A

In view of (32) and using differentiable  $p_{ar}(f_{pr})$  in (10) with differentiable  $f_{p3r}$  in (54), the chamber A control is designed as

$$\begin{aligned} u_{v31d} &= \frac{\hat{A}_{a3}}{\hat{\beta}_r} \dot{p}_{a3r} + \hat{A}_{a3} \frac{\dot{x}_3}{x_3} + k_{p31} (p_{a3r} - p_{a3}) + k_{x31} (\dot{x}_{3r} - \dot{x}_3) \\ &= \mathbf{Y}_{d31} \hat{\boldsymbol{\theta}}_{d31} + k_{p31} (p_{a3r} - p_{a3}) + k_{x31} (\dot{x}_{3r} - \dot{x}_3) \end{aligned} \quad (57)$$

where  $k_{p31}, k_{x31} > 0$ . The regressor vector  $\mathbf{Y}_{d31} \in \mathbb{R}^{1 \times 2}$  and the parameter vector  $\boldsymbol{\theta}_{d31} \in \mathbb{R}^2$  are given in Appendix E.

Then, in view of (36), the control law for the control valve of chamber A can be written as

$$u_{31} = \frac{x_3 S(u_{v31d})}{\hat{c}_{p1} v(p_s - p_{a3})} u_{v31d} + \frac{x_3 S(-u_{v31d})}{\hat{c}_{n1} v(p_{a3} - p_r)} u_{v31d} \quad (58)$$

where  $\hat{c}_{p1}$  and  $\hat{c}_{n1}$  are updated parameters for  $c_{p1}$  and  $c_{n1}$ .

When Assumptions 1 and 2 hold, the control law (58) can be inversely written, in view of (34), as

$$u_{v31d} = -\mathbf{Y}_{v31} \hat{\boldsymbol{\theta}}_{v31}. \quad (59)$$

The estimated parameter vectors  $\hat{\boldsymbol{\theta}}_{d31}$  and  $\hat{\boldsymbol{\theta}}_{v31}$  need to be updated. Define

$$\mathbf{s}_{d31} = (p_{a3r} - p_{a3}) \mathbf{Y}_{d31}^T \quad (60)$$

$$\mathbf{s}_{v31} = (p_{a3r} - p_{a3}) \mathbf{Y}_{v31}^T. \quad (61)$$

Then, the  $\gamma$ th elements of  $\hat{\boldsymbol{\theta}}_{d31}$  and  $\hat{\boldsymbol{\theta}}_{v31}$  are updated, using the  $\mathcal{P}$  function in Appendix D, as

$$\hat{\theta}_{d31\gamma} = \mathcal{P}(\mathbf{s}_{d31\gamma}, \rho_{d31\gamma}, \underline{\theta}_{d31\gamma}, \bar{\theta}_{d31\gamma}, t), \quad \forall \gamma \in \{1, 2\} \quad (62)$$

$$\hat{\theta}_{v31\gamma} = \mathcal{P}(\mathbf{s}_{v31\gamma}, \rho_{v31\gamma}, \underline{\theta}_{v31\gamma}, \bar{\theta}_{v31\gamma}, t), \quad \forall \gamma \in \{1, 2\} \quad (63)$$

where, by substituting  $(\cdot)_k$  for  $(\cdot)_{d31}$  and  $(\cdot)_{v31}$ ,  $\hat{\theta}_{k\gamma}$  is the  $\gamma$ th element of  $\hat{\boldsymbol{\theta}}_k$ ;  $\mathbf{s}_{k\gamma}$  is the  $\gamma$ th element of  $\mathbf{s}_k$ ;  $\rho_{k\gamma} > 0$  is the update gain; and  $\underline{\theta}_{k\gamma}$  and  $\bar{\theta}_{k\gamma}$  are the lower and upper bounds of  $\theta_{k\gamma}$ .

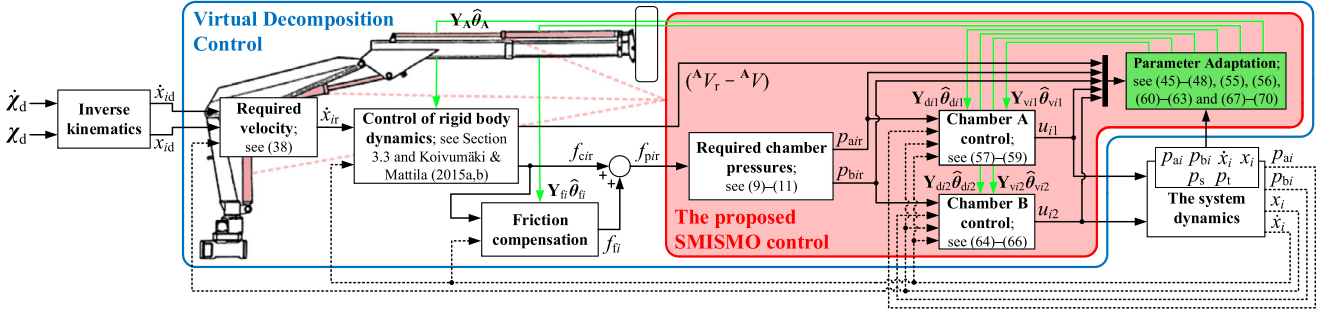


Fig. 6. The diagram of the proposed controller. The VDC controller is outlined in blue. The proposed adaptive SMISMO controller (for the system actuators) is outlined in red. The system feedback variables are shown in the dashed line. Inputs  $x_d$  and  $\dot{x}_d$  are desired Cartesian position and velocity trajectories. (For interpretation of colors in this figure, the reader is referred to the web version of this article.)

**Remark 4.** Subject to chamber A control, term  $-A_{a3}(p_{a3r} - p_{a3})(\dot{x}_{3r} - \dot{x}_3)$  is designed for the time derivative  $\dot{v}_{a3}$  of the non-negative accompanying function  $v_{a3}$ ; see (G.2) in Lemma 5 in Appendix G. This term is a part of a stabilizing counterpart for the stability preventing term in (F.2) in Lemma 4. Another stabilizing counterpart is designed next in the below.

#### Control of chamber B

In view of (33) and using differentiable  $p_{br}(f_{pr})$  in (11) with differentiable  $f_{p3r}$  in (54), the chamber B control is designed as

$$\begin{aligned} u_{v32d} &= \frac{\hat{A}_{b3}}{\beta_f} \dot{p}_{b3r} - \hat{A}_{b3} \frac{\dot{x}_3}{s_3 - x_3} + k_{p32}(p_{b3r} - p_{b3}) - k_{x32}(\dot{x}_{3r} - \dot{x}_3) \\ &= Y_{d32} \hat{\theta}_{d32} + k_{p32}(p_{b3r} - p_{b3}) - k_{x32}(\dot{x}_{3r} - \dot{x}_3) \end{aligned} \quad (64)$$

where  $k_{p32}, k_{x32} > 0$ . The regressor vector  $Y_{d32} \in \mathbb{R}^{1 \times 2}$  and the parameter vector  $\theta_{d32} \in \mathbb{R}^2$  are given in Appendix E.

Then, in view of (37), the control law for the control valve of chamber B can be written as

$$u_{32} = \frac{(s_3 - x_3)S(u_{v32d})}{\hat{c}_{p2}(p_s - p_{b3})} u_{v32d} + \frac{(s_3 - x_3)S(-u_{v32d})}{\hat{c}_{n2}(p_{b3} - p_r)} u_{v32d} \quad (65)$$

where  $\hat{c}_{p2}$  and  $\hat{c}_{n2}$  are updated parameters for  $c_{p2}$  and  $c_{n2}$ .

When Assumptions 1 and 2 hold, the control law (65) can be inversely written, in view of (35), as

$$u_{v32d} = -Y_{v32} \hat{\theta}_{v32}. \quad (66)$$

The estimated parameter vectors  $\hat{\theta}_{d32}$  and  $\hat{\theta}_{v32}$  need to be updated. Define

$$s_{d32} = (p_{b3r} - p_{b3}) Y_{d32}^T \quad (67)$$

$$s_{v32} = (p_{b3r} - p_{b3}) Y_{v32}^T. \quad (68)$$

The  $\gamma$ th elements of  $\hat{\theta}_{d32}$  and  $\hat{\theta}_{v32}$  are updated, using the  $\mathcal{P}$  function in Appendix D, as

$$\hat{\theta}_{d32\gamma} = \mathcal{P}(s_{d32\gamma}, \rho_{d32\gamma}, \bar{\theta}_{d32\gamma}, \bar{\theta}_{d32\gamma}, t), \quad \forall \gamma \in \{1, 2\} \quad (69)$$

$$\hat{\theta}_{v32\gamma} = \mathcal{P}(s_{v32\gamma}, \rho_{v32\gamma}, \bar{\theta}_{v32\gamma}, \bar{\theta}_{v32\gamma}, t), \quad \forall \gamma \in \{1, 2\} \quad (70)$$

where, by substituting  $(\cdot)_k$  for  $(\cdot)_{d32}$  and  $(\cdot)_{v32}$ ,  $\hat{\theta}_{k\gamma}$  is the  $\gamma$ th element of  $\hat{\theta}_k$ ;  $s_{k\gamma}$  is the  $\gamma$ th element of  $s_k$ ;  $\rho_{k\gamma} > 0$  is the update gain; and  $\bar{\theta}_{k\gamma}$  and  $\bar{\theta}_{k\gamma}$  are the lower and upper bounds of  $\theta_{k\gamma}$ .

Note that the following holds for required piston force

$$f_{p3r} = A_{a3} p_{a3r} - A_{b3} p_{b3r} \quad (71)$$

due to the use of (10) and (11), which satisfy Condition 2.

Fig. 6 shows the diagram for the proposed controller. The control theoretical contribution of this study is outlined in red. Note that the system structural multibody dynamics is addressed inside the block “Control of rigid body dynamics”.

**Remark 5.** Subject to chamber B control, term  $A_{b3}(p_{b3r} - p_{b3})(\dot{x}_{3r} - \dot{x}_3)$  is designed for the time derivative  $\dot{v}_{b3}$  of the non-negative accompanying function  $v_{b3}$ ; see (H.2) in Appendix H. This term is another part of the stabilizing counterpart for the stability preventing term in (F.2) in Lemma 4. Then, as Lemma 7 in Appendix I shows, the stabilizing counterpart  $-(f_{c3r} - f_{c3})(\dot{x}_{3r} - \dot{x}_3)$  can be designed for the stability preventing term  $(f_{c3r} - f_{c3})(\dot{x}_{3r} - \dot{x}_3)$ .

#### 4. Stability analysis

Virtual power flows (VPFs), defined in Appendix C, are a unique feature of VDC. The virtual stability (Definition 3 in Appendix C) of every subsystem ensures that at every VCP, a positive VPF (at a driven VCP) is connected to its corresponding negative VPF (at a driving VCP) in the adjacent subsystem. Thus, VPFS act as stability connectors between subsystems and, when all subsystems qualify as virtually stable, all the VPFS cancel each other out, eventually, leading to  $L_2$  and  $L_\infty$  stability (Lemma 1 in Appendix B) of the entire system.

Consider the hydraulic actuator assembly control design (composing of open chain 5 dynamics and cylinder 3 fluid dynamics) in Sections 3.3 and 3.4, with the dynamic properties in Lemmas 4–7 (in Appendices F–I). Theorem 1 ensures that the hydraulic actuator assembly qualifies as virtually stable.

**Theorem 1.** Consider the hydraulic actuator assembly, composing of open chain 5 control dynamics (addressed in Lemma 4) and the hydraulic cylinder control dynamics (addressed in Lemma 7), and having one driven VCP associated to VCP 5 and one driving VCP associated to VCP 6 (see Fig. 4(c)). This subsystem qualifies as virtually stable with its affiliated vector  $(^A V_r - ^A V)$ ,  $\forall A \in \Psi_{oc5}$ , and its affiliated scalar variables  $(p_{a3r} - p_{a3})$  and  $(p_{b3r} - p_{b3})$  being virtual functions in both  $L_2$  and  $L_\infty$  in the sense of Definition 3 in Appendix C. This is because, using Lemmas 4 and 7, a non-negat. accompanying function

$$\begin{aligned} v_5 \geq & \frac{1}{2} \sum_{A \in \Psi_{oc5}} (^A V_r - ^A V)^T M_A (^A V_r - ^A V) \\ & + \frac{A_{a3}^2}{2\beta_f k_{x31}} (p_{a3r} - p_{a3})^2 + \frac{A_{b3}^2}{2\beta_f k_{x32}} (p_{b3r} - p_{b3})^2 \end{aligned} \quad (72)$$

can be found such that

$$\begin{aligned} \dot{v}_5 \leq & - \sum_{A \in \Psi_{oc5}} (^A V_r - ^A V)^T K_A (^A V_r - ^A V) + p_{B5} - p_{T5} \\ & - A_{a3} \frac{k_{p31}}{k_{x31}} (p_{a3r} - p_{a3})^2 - A_{b3} \frac{k_{p32}}{k_{x32}} (p_{b3r} - p_{b3})^2 \end{aligned} \quad (73)$$

holds, where set  $\Psi_{oc5}$  contains frames  $\{B_5\}$  and  $\{B_{51}\}$ , and  $p_{B5}$  and  $p_{T5}$  are the VPFS at the (driven) VCP 5 and (driving) VCP 6 of the subsystem.

**Proof.** The proof for Theorem 1 is given in Appendix J. ■

Theorem 2 ensures that the remaining subsystem, delimited with a dashed line in Fig. 4(c), qualifies as virtually stable.



**Theorem 2.** Consider the remaining subsystem, composing of objects 0–2 and open chains 1–4, and having one driving VCP associated to VCP 5 (see Fig. 4(c)). This subsystem qualifies as virtually stable with its affiliated vector  $(^A V_r - ^A V)$ ,  $\forall A \in \Psi_r$ , and its affiliated scalar variables  $(p_{air} - p_{ai})$  and  $(p_{bir} - p_{bi})$  for the actuator  $i$ ,  $\forall i \in \{1, 2\}$ , being virtual functions in both  $L_2$  and  $L_\infty$  in the sense of Definition 3 (in Appendix C). This is because a non-negative accompanying function

$$v_R \geq \frac{1}{2} \sum_{A \in \Psi_r} (^A V_r - ^A V)^T M_A (^A V_r - ^A V) + \frac{1}{2} \sum_{i=1}^2 \left[ \frac{A_{ai}^2}{\beta_f k_{xi1}} (p_{air} - p_{ai})^2 + \frac{A_{bi}^2}{\beta_f k_{xi2}} (p_{bir} - p_{bi})^2 \right] \quad (74)$$

can be found such that

$$\dot{v}_R \leq - \sum_{A \in \Psi_r} (^A V_r - ^A V)^T K_A (^A V_r - ^A V) - p_{B_{O_2}} - \sum_{i=1}^2 \left[ A_{ai} \frac{k_{pi1}}{k_{xi1}} (p_{air} - p_{ai})^2 + A_{bi} \frac{k_{pi2}}{k_{xi2}} (p_{bir} - p_{bi})^2 \right] \quad (75)$$

holds, where set  $\Psi_r$  contains rigid body frames of the rigid links and objects in the remaining subsystem and  $p_{B_{O_2}}$  denotes VPF at the (driving) VCP 5 of this subsystem.

**Proof.** The proof for Theorem 2 can be obtained by using the results in Koivumäki and Mattila (2015b) (for objects 0–2 and open chains 2 and 4) and in Theorem 1 (for actuated open chains 1 and 3). ■

Theorem 3 ensures that object 3 qualifies as virtually stable.

**Theorem 3.** Consider object 3, having one driven VCP associated to VCP 6 (see Fig. 4(c)). This subsystem qualifies as virtually stable with its affiliated vector  $(^{O_3} V_r - ^{O_3} V)$  being a virtual function in both  $L_2$  and  $L_\infty$  in the sense of Definition 3 (in Appendix C). This is because a non-negative accompanying function

$$v_{O_3} \geq \frac{1}{2} (^{O_3} V_r - ^{O_3} V)^T M_{O_3} (^{O_3} V_r - ^{O_3} V) \quad (76)$$

can be found such that

$$\dot{v}_{O_3} \leq - (^{O_3} V_r - ^{O_3} V)^T K_{O_3} (^{O_3} V_r - ^{O_3} V) + p_{T_{O_3}} - p_G \quad (77)$$

holds, where  $p_{T_{O_3}}$  denotes the VPF at the (driven) VCP 6, and

$$p_G = (G V_r - G V)^T (G F_r - G F) = 0 \quad (78)$$

holds in the manipulator free-space motions (zero end-effector force  $\rightarrow G F_r = 0$  and  $G F = 0$ ).

**Proof.** The proof for Theorem 3 (the virtual stability of object 3) is trivial and is similar to those in Koivumäki and Mattila (2015a) and Zhu (2010). ■

In view of (14), (17), (20), (23), (39), (42), (49), (52) and (C.1) in Appendix C, the following relations hold for the VPFs at the VCPs of the hydraulic cylinder assembly:

$$p_{B_{O_2}} = p_{B_5} \quad (79)$$

$$p_{T_{O_3}} = p_{T_5} \quad (80)$$

Theorem 4 provides the stability of the entire system.

**Theorem 4.** Using (72), (74) and (76), the non-negative accompanying function for the entire system can be written as

$$v_{tot} = v_R + v_5 + v_{O_3} \geq \frac{1}{2} \sum_{A \in \Phi} (^A V_r - ^A V)^T M_A (^A V_r - ^A V) + \frac{1}{2} \sum_{i=1}^3 \left[ \frac{A_{ai}^2}{\beta_f k_{xi1}} (p_{air} - p_{ai})^2 + \frac{A_{bi}^2}{\beta_f k_{xi2}} (p_{bir} - p_{bi})^2 \right] \quad (81)$$

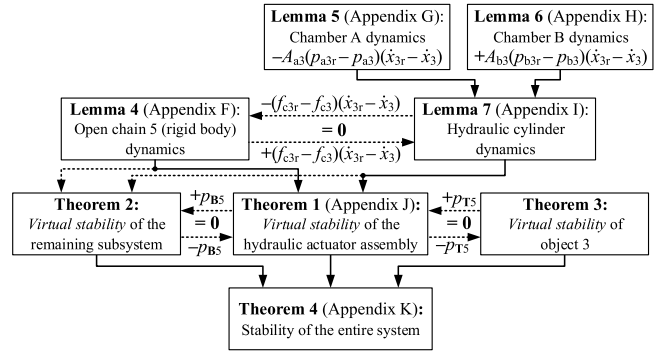


Fig. 7. The interconnections between the lemmas and theorems for the stability of the entire system.

where set  $\Phi$  contains frame  $\{O_3\}$  and sets  $\Psi_{oc5}$  and  $\Psi_r$ . Then, in view of (73), (75) and (77)–(80), the time derivative of  $v_{tot}$  can be written as

$$\begin{aligned} \dot{v}_{tot} &= \dot{v}_R + \dot{v}_5 + \dot{v}_{O_3} \\ &\leq - \sum_{A \in \Phi} (^A V_r - ^A V)^T K_A (^A V_r - ^A V) \\ &\quad - \sum_{i=1}^3 \left[ A_{ai} \frac{k_{pi1}}{k_{xi1}} (p_{air} - p_{ai})^2 + A_{bi} \frac{k_{pi2}}{k_{xi2}} (p_{bir} - p_{bi})^2 \right]. \end{aligned} \quad (82)$$

Finally, in view of Lemmas 1 and 2 (in Appendix B), (81) and (82), it follows that  $(^A V_r - ^A V) \in L_2 \cap L_\infty, \forall A \in \Phi$ ,  $(p_{air} - p_{ai}) \in L_2 \cap L_\infty$ ,  $(p_{bir} - p_{bi}) \in L_2 \cap L_\infty$ ,  $(\dot{x}_{ir} - \dot{x}_i) \in L_2 \cap L_\infty$ ,  $(\dot{x}_{id} - \dot{x}_i) \in L_2 \cap L_\infty$ , and  $(x_{id} - x_i) \in L_2 \cap L_\infty$  hold,  $\forall i \in \{1, 2, 3\}$ , leading to the stability of the entire system.

**Proof.** The proof for Theorem 4 is given in Appendix K. ■

Fig. 7 shows the control design procedure for the stability of the entire system. In short, open chain 5 control creates a stability-preventing term  $(f_{c3r} - f_{c3})(\dot{x}_{3r} - \dot{x}_3)$  in Lemma 4. Then, such chamber pressure controls are designed (whose control dynamics are addressed in Lemmas 5 and 6) that a stabilizing counterpart  $-(f_{c3r} - f_{c3})(\dot{x}_{3r} - \dot{x}_3)$  will appear in Lemma 7. Using Lemmas 4 and 7, it can be shown that the hydraulic actuator assembly qualifies as virtually stable (in Theorem 1). Then, all VPFs among the subsystems cancel each other out (see Theorems 1–3 in Fig. 7). Eventually, the entire system qualifies as  $L_2$  and  $L_\infty$  stable in view of Theorem 4.

An asymptotic convergence of the proposed controller can be addressed as shown in Remark 6.

**Remark 6.** Let the desired piston position  $x_{id}$  be a continuously differentiable function in  $C^2$ , i.e.,  $\{x_{id}, \dot{x}_{id}, \ddot{x}_{id}, x_{id}^{(3)}\} \in L_\infty$  holds. Then, Lemma 3 in Appendix B can be used to prove the asymptotic convergence of the designed controller. Following the procedure presented in Zhu (2010), it can be shown that  $(^A V_r - ^A V) \in L_\infty, \forall A \in \Phi$ ,  $(\dot{p}_{air} - \dot{p}_{ai}) \in L_\infty$ ,  $(\dot{p}_{bir} - \dot{p}_{bi}) \in L_\infty$ ,  $(\ddot{x}_{id} - \ddot{x}_i) \in L_\infty$ , and  $(\dot{x}_{id} - \dot{x}_i) \in L_\infty$  hold, leading to asymptotic convergence of the feedback signals in view of Lemma 3.

## 5. Experiments

This section demonstrates the performance of the proposed SMISMO control. Section 5.1 outlines the system implementation issues. Section 5.2 presents the results with the SMISMO control in relation to the conventional servovalve control. Section 5.3 evaluates the SMISMO control performance with respect to the state-of-the-art solutions. Section 5.4 evaluates the energy consumption reductions with the SMISMO control.

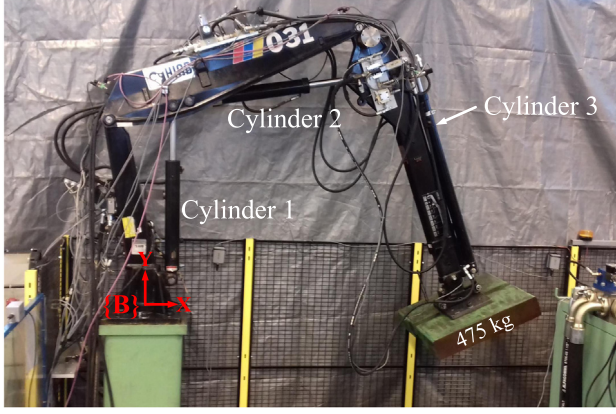


Fig. 8. The experimental set-up. The manipulator's base frame {B} is shown in red. The manipulator's position in this figure shows the starting point of the driven motion trajectories. (For interpretation of colors in this figure, the reader is referred to the web version of this article.)

### 5.1. Experiment set-up and implementation issues

The studied three-DOF redundant manipulator is shown in Fig. 8. The maximum reach of the manipulator is approximately 4.2 m. The payload of 475 kg is attached to the manipulator. For cylinders 1 and 2, Bosch 4WRPEH10 proportional valves (bandwidth of 100 Hz and 100 dm<sup>3</sup>/min @  $\Delta p = 35$  bar per notch) were used to realize the SMISMO control; for cylinder 3, Bosch 4WRPEH6 proportional valves (bandwidth of 100 Hz and 40 dm<sup>3</sup>/min @  $\Delta p = 35$  bar per notch) were used. The remaining of the system is identical to that described in Koivumäki and Mattila (2015a). The hardware for the conventional servovalve control set-up was identical to the above; however, only one control valve per cylinder was used (as shown in Fig. 1). Hereinafter, the *conventional control* denotes the VDC control design for the studied system employing one control valve per cylinder.

The sample time of control system was set to 3 ms (the turnaround time was  $\approx 2.8$  ms). The actuators' feedback gains are shown in Table 1. As in the conventional control, the piston force is controlled, whereas, in the SMISMO control, also the chamber pressures are controlled, thus, the gains are not exactly same. The same parameter update gains were used to update the rigid body parameters and the friction parameters in the conventional and the SMISMO controls. Due to the different actuator control designs, regressors (and parameter update gains) were not exactly same to update the actuators' parameters.<sup>5</sup> For the importance of a parameter adaptation and the effect of the parameter adaptation law (D.1) (see Appendix D) to the high-precision tracking control with hydraulic systems, interested readers are referred to Koivumäki and Mattila (2017b) and Zhu and Piedboeuf (2005). In the control, the same first-order filter as, e.g., in Koivumäki and Mattila (2015a) and Koivumäki et al. (2014), was used for the chamber pressure measurements to eliminate sensor noises. The choice of the filter is to make sure that considerable phase lags only happen at frequencies beyond the range of the system dynamics. All data in Figs. 9–14 are raw (unfiltered) data.

The applicable motion (velocity) specifications of the system are directly related to the sizes of the control valves (the flow coefficients  $c_{p1}$ ,  $c_{n1}$ ,  $c_{p2}$  and  $c_{n2}$ ) and the pressure differences across the valves; see (28) and (29). In the SMISMO control, the pressure difference across the valves is intended to be minimized with  $\Delta p_c$  (which also defines

Table 1

Actuator space feedback gains.

Conventional hydraulic cylinder control; see (76) and (111) in Koivumäki and Mattila (2015a).			
	Cylinder 1	Cylinder 2	Cylinder 3
$\lambda_i$ [m/s]:	30	34	27
$k_{fi}$ [m <sup>2</sup> /(N·s)]:	$6.0 \cdot 10^{-8}$	$8.0 \cdot 10^{-8}$	$20.0 \cdot 10^{-8}$
$k_{xi}$ [m]:	0.030	0.030	0.028
The proposed SMISMO control; see (38), (57), and (64).			
	Cylinder 1	Cylinder 2	Cylinder 3
$\lambda_i$ [m/s]:	32	28	26
$k_{pi1}$ [m <sup>2</sup> /(Pa·s)]:	$5 \cdot 10^{-10}$	$3.0 \cdot 10^{-10}$	$5.0 \cdot 10^{-10}$
$k_{pi2}$ [m <sup>2</sup> /(Pa·s)]:	$4 \cdot 10^{-10}$	$1.4 \cdot 10^{-10}$	$2.1 \cdot 10^{-11}$
$k_{xi1}$ [m]:	0.020	0.026	0.010
$k_{xi2}$ [m]:	0.020	0.005	0.002

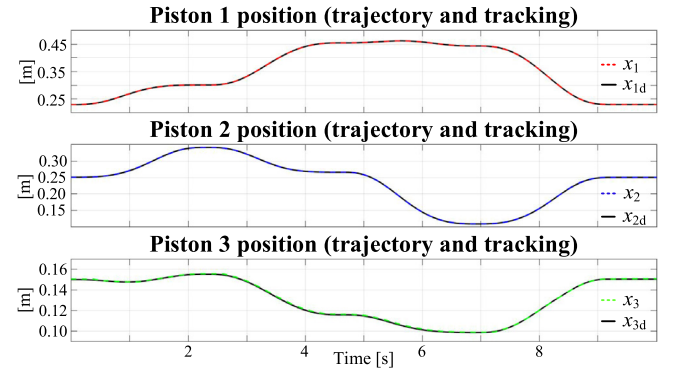


Fig. 9. The piston position trajectories produced by the driven Cartesian motion trajectory in black. The measured piston position with the SMISMO control are shown in red, blue and green. Note the different scale in the y-axes. (For interpretation of colors in this figure, the reader is referred to the web version of this article.)

the desired minimum pressure level for the cylinders' chambers; see Sections 2.2 and 2.3). Such a value for  $\Delta p_c$  should be used such that cavitation and control valve saturation are avoided, and the intended motion specifications (depending on the *fixed* flow coefficients and *adjustable*  $\Delta p_c$ ) can be obtained. In the experiments,  $\Delta p_c = 20$  bar is used for all cylinders to ensure the use of sufficiently fast velocity trajectory (the maximum Cartesian velocity of 0.9 m/s).

### 5.2. The experimental results

In Figs. 9–13, similar colors as in Fig. 4 are used to depict the cylinder variables; i.e., cylinders 1–3 variables are shown in red, blue and green, respectively. The reference trajectories (if any) are shown in black. In the experiments, the same parallelogram Cartesian point-to-point path (height in Y-axis 2 m, length in X-axis 1 m) as in Koivumäki and Mattila (2015a) was driven with the *conventional control* and with the SMISMO control. A quintic rest-to-rest trajectory generator was used to generate the desired motion trajectories between the corner points. The transition time between two points was set to 2.3 s. The piston position trajectories, produced by the trajectory generator (Koivumäki & Mattila, 2015a), are shown in Fig. 9 and their position trackings with the SMISMO control are shown in red, blue and green. The detailed position tracking errors with the *conventional control* and the SMISMO control are shown later in Figs. 10 and 12. In the experiments, a constant displacement pump with a supply pressure of 200 bar was used.

#### Tracking results with the conventional control

Figs. 10–11 show the results with the *conventional control*. The first plot in Fig. 10 shows the piston position tracking errors during the test trajectory. The maximum absolute tracking errors are  $|e_1|_{\max} = 0.70$  mm,  $|e_2|_{\max} = 0.57$  mm, and  $|e_3|_{\max} = 0.98$  mm for pistons 1–3, respectively.

<sup>5</sup> In the conventional control,  $s_{di} = (f_{pir} - f_{pi})Y_{di}^T$  and  $s_{vi} = (f_{pir} - f_{pi})Y_{vi}^T$  are used to update the fluid dynamics parameters and the valve flow coefficients (see Koivumäki & Mattila, 2015b), whereas  $s_{d31}$ ,  $s_{v31}$ ,  $s_{d32}$  and  $s_{v32}$  in (60), (61), (67), and (68), respectively, are used to update the fluid dynamics parameters and the valve flow coefficients in the SMISMO control.

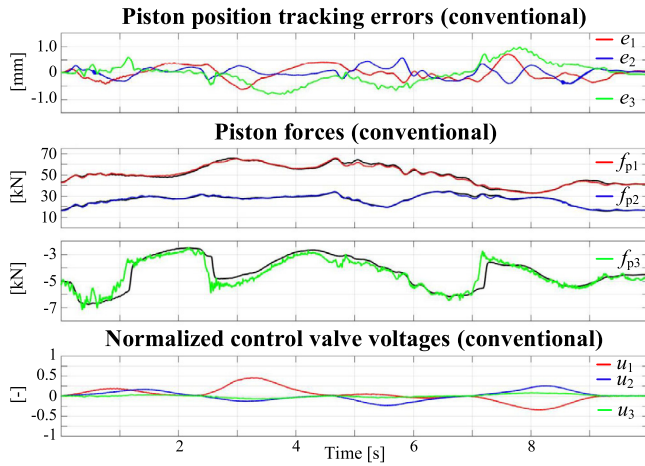


**Fig. 10.** The conventional hydraulic cylinder control. The first plot shows the piston position tracking error for cylinders 1–3. The middle plots show the measured piston forces for cylinders 1–3. The required piston force trajectories are shown in black. The last plot shows the normalized control valve voltages. (For interpretation of colors in this figure, the reader is referred to the web version of this article.)

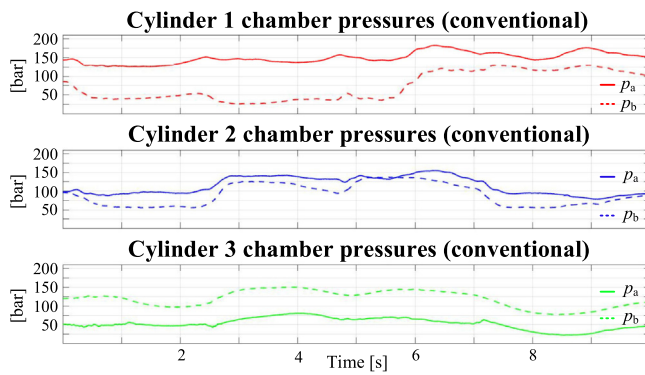


**Fig. 11.** The chamber pressures with the conventional hydraulic cylinder control. For all cylinders, the chamber A pressure is given in the solid line, and the chamber B pressure is given in the dashed line. (For interpretation of colors in this figure, the reader is referred to the web version of this article.)

The respective maximum absolute piston velocities in the test trajectory were  $|\dot{x}_1|_{\max} = 0.180$  m/s,  $|\dot{x}_2|_{\max} = 0.135$  m/s, and  $|\dot{x}_3|_{\max} = 0.040$  m/s. The second and third plots show the piston force tracking for the pistons. The last plot shows the normalized control valve voltages for the cylinders' control valves.

**Fig. 11** shows the chamber pressures of the cylinders in the *conventional control*. The solid lines are for chamber A pressures, and the dashed lines are for chamber B pressures. As discussed, in the conventional control, only the piston forces are controllable, whereas the individual chamber pressures are not. Thus, no pressure trajectories exist in **Fig. 11**.

#### Tracking results with the smismo control

**Figs. 12** and **13** show the results with the *SMISMO control*. The first plot in **Fig. 12** shows the piston position tracking errors during the test trajectory. As the plot shows, very similar piston position tracking behaviors are obtained in relation to the *conventional control* (see relation to **Fig. 10**). The maximum absolute tracking errors are  $|e_1|_{\max} = 0.54$  mm,  $|e_2|_{\max} = 0.81$  mm, and  $|e_3|_{\max} = 1.00$  mm for pistons 1–3, respectively. The respective maximum absolute piston velocities in the test trajectory were  $|\dot{x}_1|_{\max} = 0.178$  m/s,  $|\dot{x}_2|_{\max} = 0.134$  m/s, and  $|\dot{x}_3|_{\max} = 0.039$  m/s. The second and third plots show the piston force tracking for pistons 1–3. As the plots show, almost an identical high-precision force trackings are obtained in relation to the *conventional control* (see the relation to **Fig. 10**). The last plot shows the normalized

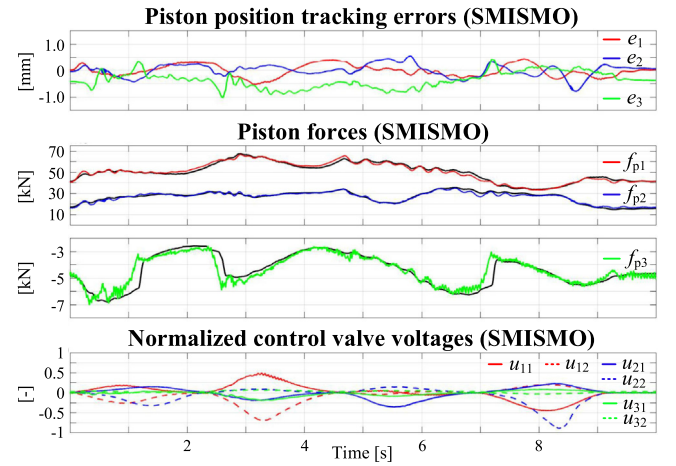


**Fig. 12.** The proposed SMISMO control. The first plot shows the piston position tracking error for cylinders 1–3. The middle plots show the measured piston forces for cylinders 1–3. The required piston force trajectories are shown in black. The last plot shows the normalized control valve voltages. (For interpretation of colors in this figure, the reader is referred to the web version of this article.)

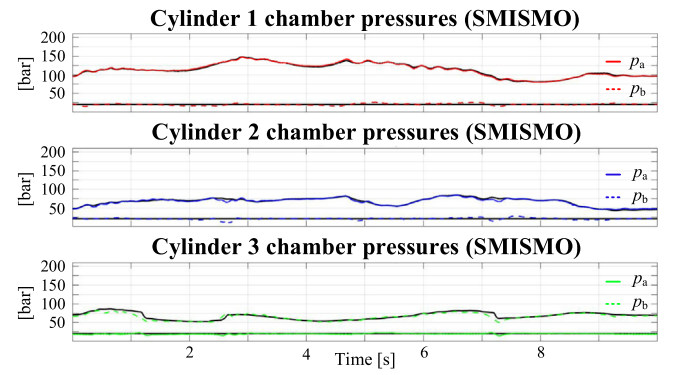


**Fig. 13.** The chamber pressures for the SMISMO control. For all cylinders, the chamber A pressure is given in the solid line, and the chamber B pressure is given in the dashed line. The required chamber pressures are given in black. (For interpretation of colors in this figure, the reader is referred to the web version of this article.)

control valve voltages for the SMISMO control valves of the cylinders. As the plot shows, the maximum achievable velocity range was used in the experiments as the maximum valve opening occurred in the driven test trajectory for one of the valves ( $u_{22}$  data in the dashed blue line).

**Fig. 13** shows the cylinders' chamber pressure trackings in the test trajectory with the *SMISMO control*. Despite the challenges (see Section 2.2), accurate pressure tracking is obtained in all chambers. The chamber pressures are substantially lowered in relation to the chamber pressures in the *conventional control* (see **Fig. 11**), although very similar piston force trackings are obtained in **Figs. 10** and **12**. As **Figs. 12** and **13** show, the triple objective of the high-precision *piston position*, *piston force* and *chamber pressures* trackings are designed.

**Table 2** shows the root mean square (RMS) pressure tracking errors  $|e_p|_{\text{RMS}}$  and the maximum absolute pressure tracking errors  $|e_p|_{\max}$  for each cylinder chamber. In addition to the superior position control performance (discussed next), an unprecedented chamber pressure tracking is obtained with the proposed SMISMO control in relation to previous pressure tracking studies; see **Figs. 7–8** in **Mattila and Virvalo (2000)** and **Figs. 8–10** in **Koivumäki and Mattila (2013)**. No detailed chamber pressure tracking is reported in **Liu and Yao (2008)** and **Lu and Yao (2014)**.



**Table 2**  
Chamber pressure tracking errors.

	Cylinder 1		Cylinder 2		Cylinder 3	
	Chamber A	Chamber B	Chamber A	Chamber B	Chamber A	Chamber B
$ e_p _{\text{RMS}}$	1.57 bar	2.37 bar	2.09 bar	2.40 bar	1.78 bar	3.82 bar
$ e_p _{\text{max}}$	4.58 bar	6.94 bar	8.74 bar	10.72 bar	6.64 bar	17.68 bar

### Cartesian motion control performances

The end-effector position-tracking accuracy is typically the most important factor in the motion control of manipulators. Fig. 14 shows the Cartesian position tracking errors (the first plot) and Cartesian velocities (the second plot) for the *conventional control* (in gray) and for the *SMISMO control* (in black) in the driven test trajectory. Very similar behaviors are obtained with these two methods. For the *conventional control*, the absolute maximum Cartesian position tracking error is  $|e_x|_{\text{max}} = 4.8$  mm, the RMS position tracking error is  $|e_x|_{\text{RMS}} = 2.7$  mm, and the maximum Cartesian velocity is  $|\dot{x}|_{\text{max}} = 0.915$  m/s. The respective values for the *SMISMO control* are  $|e_x|_{\text{max}} = 5.2$  mm,  $|e_x|_{\text{RMS}} = 2.6$  mm, and  $|\dot{x}|_{\text{max}} = 0.920$  m/s. The position tracking accuracies can be considered a significant result in the light of the manipulator scale (the maximum reach of  $\approx 4.2$  m).

### 5.3. Motion control performance evaluation

To promote the scientific cornerstones of reproducible and measurable research (see Bonsignorio & del Pobal, 2015), the following normalizing performance indicator  $\rho$  from Zhu et al. (2013), Zhu and Piedboeuf (2005) and Zhu and Vukovich (2011) is used for the motion control performance evaluation

$$\rho = \frac{\max(|x_{\text{des}} - x|)}{\max(|\dot{x}|)} = \frac{|e|_{\text{max}}}{|\dot{x}|_{\text{max}}} \quad (83)$$

where  $x_{\text{des}}$  is the desired position and  $x$  is the measured position. The index quantifies the tracking control performance of a robot. The index is expressed in seconds (s), which is the inverse of the bandwidth. Thus, the smaller the  $\rho$ , the better the performance. The rationale for selecting this index is that usually large velocities in the task space are associated with large accelerations, which, in turn, result in large position tracking errors considering the uncertainties in robot dynamics (Zhu et al., 2013).

Using data in Fig. 14,  $\rho = \frac{0.0048 \text{ m}}{0.915 \text{ m/s}} \approx 0.0052$  (s) can be measured for the *conventional control* in the Cartesian space. For the *proposed SMISMO control*,  $\rho = \frac{0.0052 \text{ m}}{0.920 \text{ m/s}} \approx 0.0057$  (s) can be measured. As the values imply, a slightly better performance indicator  $\rho$  value is achieved with the conventional control; however, the difference to the proposed SMISMO control is minor. The state-of-the-art in Cartesian motion tracking for hydraulic robotic manipulators using conventional servovalve control are reported in Mattila et al. (2017, Table II). From the data in Mattila et al. (2017), only the VDC-based controller (Koivumäki & Mattila, 2015a) reports a better Cartesian space performance indicator value ( $\rho = 0.0050$  s) in relation to the proposed controller, whereas the other methods are far behind.

Table 3 shows the performance indicator values in the *actuator space* for SMISMO control methods of hydraulic robotic manipulators; no Cartesian space data available in Koivumäki and Mattila (2013), Liu and Yao (2008), Lu and Yao (2014) and Mattila and Virvalo (2000). The performance indicators are reported for the best actuator. The abbreviation DOF in the last column of Table 3 denotes the number of driven actuators in the experiments. Note that in Liu and Yao (2008) and Lu and Yao (2014) only one actuator was driven in the experiments, disabling cross-coupled dynamics between the links. As Table 3 shows, the proposed controller achieves the best performance indicator value in relation to Koivumäki and Mattila (2013), Liu and Yao (2008), Lu and Yao (2014) and Mattila and Virvalo (2000). It is valid to mention that the controllers in Liu and Yao (2008) and Lu and Yao (2014) used cartridge valves (with a natural frequency of 353.6 rad/s) instead of

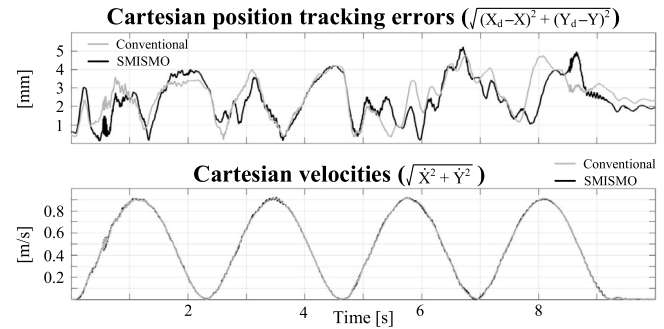


**Fig. 14.** The Cartesian motion data for the conventional control (in gray) and for the proposed SMISMO control (in black). The first plot shows the Cartesian position tracking error profiles in the driven test trajectory. The second plot shows the Cartesian velocity profiles.

**Table 3**

The actuator space performance indicator values for SMISMO control of hydraulic robotic manipulators.

Study	$\rho$ [s]	DOF
<b>This study</b>	<b>0.0030</b>	<b>3</b>
Koivumäki 2013 (Koivumäki & Mattila, 2013)	0.0055	2
Liu 2008 (Liu & Yao, 2008)	0.0072 <sup>a</sup>	1 <sup>b</sup>
Mattila 2000 (Mattila & Virvalo, 2000)	0.0130	2
Lu 2014 (Lu & Yao, 2014)	0.0280 <sup>a</sup>	1 <sup>b</sup>

<sup>a</sup>The maximum absolute velocity  $|\dot{x}|_{\text{max}}$  was not reported; the maximum absolute desired velocity  $|\dot{x}_d|_{\text{max}}$  was used instead.

<sup>b</sup>Three-DOF hydraulic arm, however, in the experiments only one of the actuators was driven.

**Table 4**

Hydraulic energy consumptions.

	Cyl1 [J]	Cyl2 [J]	Cyl3 [J]	Total [J]
Conventional	$2.56 \times 10^4$	$2.10 \times 10^4$	$1.44 \times 10^3$	$4.80 \times 10^4$
SMISMO	$1.64 \times 10^4$	$0.93 \times 10^4$	$0.71 \times 10^3$	$2.64 \times 10^4$

servovalves used in the other studies. Finally, in relation to the best measured actuator space motion tracking accuracy reported in Mattila et al. (2017, Table I), the very same performance indicator value ( $\rho = 0.0030$  s) is obtained with the proposed SMISMO control.

### 5.4. Energy consumption evaluation

The hydraulic energy  $E_{\text{ha}}$  consumed by an actuator can be written as

$$E_{\text{ha}} = \int_{t_0}^{t_1} Q_{\text{in}}(\tau) p_{\text{in}}(\tau) d\tau \quad (84)$$

where  $Q_{\text{in}}$  is the fluid flow rate taken from the supply line and  $p_{\text{in}}$  is the pressure of the meter-in chamber.

Table 4 shows the hydraulic energy consumed by cylinders 1–3 during the test trajectory (from  $t_0 = 0$  to  $t_1 = 10$ ) with the conventional control and the SMISMO control. The last column shows the total hydraulic energy consumed by all the actuators. In relation to the *conventional control*, the energy consumption of cylinders 1–3 is reduced by 35.9%, 55.7% and 50.7%, respectively, with the SMISMO control. The total energy consumption of all the cylinders is reduced by 45.0% with the SMISMO control. Finally, Fig. 15 shows the total energy consumption curves with the *conventional control* (in gray) and the *SMISMO control* (in black).

Table 4 and Fig. 15 demonstrate the maximum potential for the energy consumption reductions with the SMISMO control in the driven test trajectory. With the current setup, the hydraulic energy is still significantly wasted through the system's control valves and pressure relief valve due to the use of a constant displacement pump. In future studies, the hydraulic manipulator (with the proposed SMISMO control)



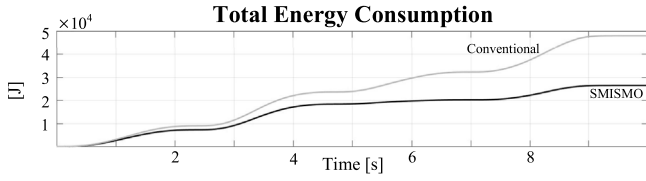


Fig. 15. The system total energy consumption for the conventional control (in gray) and for the proposed SMISMO control (in black).

will be coupled to an electro-hydraulically controlled variable displacement pump (see Koivumäki & Mattila, 2017b,c) to further investigate the system's total energy consumption reduction. The highly complex dynamic interactions between these two systems will be addressed by using the tools provided by VDC and the method in Koivumäki and Mattila (2017b).

## 6. Conclusions

This study addressed a challenging problem of improving *energy efficiency* of hydraulic *n*-DOF robotic systems without losing a *high-precision control performance* needed in robotic tasks. For energy efficiency, a SMISMO-control setup was used for individual metering control of the chambers of hydraulic actuators, and energy consumption optimizing chamber pressure trajectories were designed. The control design principles of the VDC approach were used (i) to virtually decompose the three-DOF redundant hydraulic robotic manipulator to modular subsystems and (ii) to design the control in the subsystem level, allowing to address hydraulic actuators' high-precision piston position, piston force and chamber pressure trackings. A rigorous stability proof for the entire system was given.

The experiments with the three-DOF hydraulic manipulator reveal that: (1) It is possible to design the triple objective of hydraulic actuators' high-precision *piston position*, *piston force* and *chamber pressure* trackings. This is demonstrated for the first time. (2) Unprecedented piston motion and chamber pressure trackings is designed in relation to previous SMISMO control methods. (3) In relation to the state-of-the-art controllers for *n*-DOF manipulators reviewed in Mattila et al. (2017), only one method (using also VDC) have reported slightly better motion control performance in view of the performance indicator  $\rho$ . (4) In relation to the *state-of-the-art controller* with the conventional energy-inefficient servovalve control, the actuators' total energy consumption is reduced by 45% (see Fig. 15) without noticeable Cartesian position-tracking accuracy lost (see Fig. 14).

Due to the possibility to improve the system energy efficiency without losing motion control accuracy, the need for an extra control valve per actuator and more complex control design can be justifiable. Furthermore, the results of the study demonstrates an important step toward energy-autonomous ambulatory hydraulic robotic systems, where the control performance cannot not sacrificed in the process of improving the system's energy efficiency.

## Conflict of interest

None declared.

## Funding

This work was supported by the Academy of Finland under the project "Autonomous grasping and centralized multimodal human machine interface for multi-site heavy-duty working machines (AUTO-GRACE)" [Grant No. 304604].

## Appendix A. Dynamics of a rigid body

Consider an orthogonal, three-dimensional coordinate system  $\{A\}$  (frame  $\{A\}$ ) attached to the rigid body. Let  ${}^A\mathbf{v} \in \mathbb{R}^3$  and  ${}^A\boldsymbol{\omega} \in \mathbb{R}^3$  be the linear and angular velocity vectors of frame  $\{A\}$ , expressed in frame  $\{A\}$ . To facilitate the transformations of velocities among different frames, the linear/angular velocity vector of frame  $\{A\}$  can be written, in view of Zhu (2010), as

$${}^A\mathbf{V} \stackrel{\text{def}}{=} [{}^A\mathbf{v} \ {}^A\boldsymbol{\omega}]^T \in \mathbb{R}^6. \quad (\text{A.1})$$

Let  ${}^A\mathbf{f} \in \mathbb{R}^3$  and  ${}^A\mathbf{m} \in \mathbb{R}^3$  be the force and moment vectors applied to the origin of frame  $\{A\}$ , expressed in frame  $\{A\}$ . Similar to (A.1), the force/moment vector in frame  $\{A\}$  can be written, in view of Zhu (2010), as

$${}^A\mathbf{F} \stackrel{\text{def}}{=} [{}^A\mathbf{f} \ {}^A\mathbf{m}]^T \in \mathbb{R}^6. \quad (\text{A.2})$$

Consider two given frames, denoted as  $\{A\}$  and  $\{B\}$ , fixed to a common rigid body. The following relations hold (Zhu, 2010):

$${}^B\mathbf{V} = {}^A\mathbf{U}_B^T {}^A\mathbf{V} \quad (\text{A.3})$$

$${}^A\mathbf{F} = {}^A\mathbf{U}_B {}^B\mathbf{F} \quad (\text{A.4})$$

where  ${}^A\mathbf{U}_B \in \mathbb{R}^{6 \times 6}$  denotes a force/moment transformation matrix that transforms the force/moment vector measured and expressed in frame  $\{B\}$  to the same force/moment vector measured and expressed in frame  $\{A\}$ ; for more details, see Zhu (2010).

Let frame  $\{A\}$  be fixed to a rigid body. The rigid body dynamics, expressed in frame  $\{A\}$ , can be written as

$$\mathbf{M}_A \frac{d}{dt} ({}^A\mathbf{V}) + \mathbf{C}_A ({}^A\boldsymbol{\omega}) {}^A\mathbf{V} + \mathbf{G}_A = {}^A\mathbf{F}^* \quad (\text{A.5})$$

where  ${}^A\mathbf{F}^* \in \mathbb{R}^6$  is the net force/moment vector of the rigid body expressed in frame  $\{A\}$ , and  $\mathbf{M}_A \in \mathbb{R}^{6 \times 6}$ ,  $\mathbf{C}_A ({}^A\boldsymbol{\omega}) \in \mathbb{R}^{6 \times 6}$  and  $\mathbf{G}_A \in \mathbb{R}^6$  are the mass matrix, the Coriolis and centrifugal matrix and the gravity vector, respectively. The detailed expressions can be found in Zhu (2010).

Now, let  ${}^A\mathbf{V}_r \in \mathbb{R}^6$  be the required vector of  ${}^A\mathbf{V} \in \mathbb{R}^6$ . In view of Zhu (2010), the linear parameterization expression for the required rigid body dynamics can be written as

$$\mathbf{Y}_A \boldsymbol{\theta}_A \stackrel{\text{def}}{=} \mathbf{M}_A \frac{d}{dt} ({}^A\mathbf{V}_r) + \mathbf{C}_A ({}^A\boldsymbol{\omega}) {}^A\mathbf{V}_r + \mathbf{G}_A. \quad (\text{A.6})$$

The detailed expressions of the regressor matrix  $\mathbf{Y}_A \in \mathbb{R}^{6 \times 13}$  and the parameter vector  $\boldsymbol{\theta}_A \in \mathbb{R}^{13}$  can be found in Zhu (2010).

## Appendix B. $L_2$ and $L_\infty$ stability

The Lebesgue space is defined as shown in Definition 1.

**Definition 1** (Zhu, 2010). The Lebesgue space, denoted as  $L_p$  with  $p$  being a positive integer, contains all Lebesgue measurable and integrable functions  $f(t)$  subject to

$$\|f\|_p = \lim_{T \rightarrow \infty} \left[ \int_0^T |f(t)|^p dt \right]^{\frac{1}{p}} < +\infty. \quad (\text{B.1})$$

Two particular cases are considered:

- (a) A Lebesgue measurable function  $f(t)$  belongs to  $L_2$  if and only if  $\lim_{T \rightarrow \infty} \int_0^T |f(t)|^2 dt < +\infty$ .
- (b) A Lebesgue measurable function  $f(t)$  belongs to  $L_\infty$  if and only if  $\max_{t \in [0, \infty)} |f(t)| < +\infty$ .

**Lemma 1** (a simplified version of Lemma 2.3 in Zhu (2010)) provides that a system is  $L_2$  and  $L_\infty$  stable with its affiliated vector  $\mathbf{x}(t)$ , being a function in  $L_\infty$  and its affiliated vector  $\mathbf{y}(t)$ , being a function in  $L_2$ .

**Lemma 1 (Zhu, 2010).** Consider a non-negative differentiable function  $\xi(t)$  defined as

$$\xi(t) \geq \frac{1}{2} \mathbf{x}(t)^T \mathbf{P} \mathbf{x}(t) \quad (\text{B.2})$$

with  $\mathbf{x}(t) \in \mathbb{R}^n$ ,  $n \geq 1$ , and  $\mathbf{P} \in \mathbb{R}^{n \times n}$  being a symmetric positive-definite matrix. If the time derivative of  $\xi(t)$  is Lebesgue integrable and governed by

$$\dot{\xi}(t) \leq -\mathbf{y}(t)^T \mathbf{Q} \mathbf{y}(t) \quad (\text{B.3})$$

where  $\mathbf{y}(t) \in \mathbb{R}^m$ ,  $m \geq 1$ , and  $\mathbf{Q} \in \mathbb{R}^{m \times m}$  being a symmetric positive-definite matrix. Then it follows that  $\xi(t) \in L_\infty$ ,  $\mathbf{x}(t) \in L_\infty$  and  $\mathbf{y}(t) \in L_2$  hold.

**Lemma 2** provides that the  $L_2$  and  $L_\infty$  signal retains its properties after passing through a first-order MIMO filter.

**Lemma 2 (Zhu, 2010).** Consider a first-order MIMO system described by

$$\dot{\mathbf{x}}(t) + \mathbf{K} \mathbf{x}(t) = \mathbf{u}(t) \quad (\text{B.4})$$

with  $\mathbf{x}(t) \in \mathbb{R}^n$ ,  $\mathbf{u}(t) \in \mathbb{R}^n$ , and  $\mathbf{K} \in \mathbb{R}^{n \times n}$  being symmetrical and positive-definite. If  $\mathbf{u}(t) \in L_2 \cap L_\infty$  holds, then  $\mathbf{x}(t) \in L_2 \cap L_\infty$ , and  $\dot{\mathbf{x}}(t) \in L_2 \cap L_\infty$  hold.

If asymptotic stability is demanded for the control system, then the well-known Barbalat lemma is typically used (Slotine & Li, 1991). **Lemma 3** provides an alternative to Barbalat's lemma.

**Lemma 3 (Tao, 1997).** If  $e(t) \in L_2$  and  $\dot{e}(t) \in L_\infty$ , then  $\lim_{t \rightarrow \infty} e(t) = 0$ .

**Remark 7.** As a distinction to Lyapunov approaches, **Lemma 1** allows different appearances of variables in the non-negative function itself and in its time-derivative. When all error signals are proven to belong to  $L_2$  and  $L_\infty$  in the sense of **Lemma 1**, then asymptotic stability can be proven with **Lemma 3**, if the time-derivatives of all error signals belong to  $L_\infty$ .

### Appendix C. Virtual stability

The unique feature of the VDC approach is the introduction of a scalar term, namely the *virtual power flow* (VPF) (Zhu, 2010); see **Definition 2**. The VPFs uniquely define the dynamic interactions among the subsystems and play an important role in the definition of *virtual stability* (Zhu, 2010), which is defined in a simplified form in **Definition 3**.

**Definition 2 (Zhu, 2010).** The *virtual power flow* with respect to frame  $\{\mathbf{A}\}$  is the inner product of the linear/angular velocity vector error and the force/moment vector error as

$$p_{\mathbf{A}} = (\mathbf{A}V_{\mathbf{r}} - \mathbf{A}V)^T (\mathbf{A}F_{\mathbf{r}} - \mathbf{A}F) \quad (\text{C.1})$$

where  $\mathbf{A}V_{\mathbf{r}} \in \mathbb{R}^6$  and  $\mathbf{A}F_{\mathbf{r}} \in \mathbb{R}^6$  represent the required vectors of  $\mathbf{A}V \in \mathbb{R}^6$  and  $\mathbf{A}F \in \mathbb{R}^6$ , respectively.

**Definition 3 (Zhu, 2010).** A subsystem with a *driven* VCP to which frame  $\{\mathbf{A}\}$  is attached and a *driving* VCP to which frame  $\{\mathbf{C}\}$  is attached is said to be *virtually stable* with its affiliated vector  $\mathbf{x}(t)$  being a virtual function in  $L_\infty$  and its affiliated vector  $\mathbf{y}(t)$  being a virtual function in  $L_2$ , if and only if there exists a non-negative accompanying function

$$v(t) \geq \frac{1}{2} \mathbf{x}(t)^T \mathbf{P} \mathbf{x}(t) \quad (\text{C.2})$$

such that

$$\dot{v}(t) \leq -\mathbf{y}(t)^T \mathbf{Q} \mathbf{y}(t) + p_{\mathbf{A}} - p_{\mathbf{C}} \quad (\text{C.3})$$

holds, where  $\mathbf{P}$  and  $\mathbf{Q}$  are two block-diagonal positive-definite matrices, and  $p_{\mathbf{A}}$  and  $p_{\mathbf{C}}$  denote the *virtual power flows* (by **Definition 2**) at frames  $\{\mathbf{A}\}$  and  $\{\mathbf{C}\}$ , respectively.

### Appendix D. Parameter adaptation

The following projection function  $\mathcal{P}$  from Zhu (2010) is used for parameter adaptation:

**Definition 4.** A projection function  $\mathcal{P}(s(t), k, a(t), b(t), t) \in \mathbb{R}$  is a differentiable scalar function defined for  $t \geq 0$  such that its time derivative is governed by

$$\dot{\mathcal{P}} = k s(t) \kappa \quad (\text{D.1})$$

with

$$\kappa = \begin{cases} 0, & \text{if } \mathcal{P} \leq a(t) \text{ and } s(t) \leq 0 \\ 0, & \text{if } \mathcal{P} \geq b(t) \text{ and } s(t) \geq 0 \\ 1, & \text{otherwise} \end{cases}$$

where  $s(t) \in \mathbb{R}$  is a scalar variable,  $k > 0$  is a constant, and  $a(t) \leq b(t)$  holds.

The projection function in (D.1) has the following property: For any constant  $\mathcal{P}_c$  subject to  $a(t) \leq \mathcal{P}_c \leq b(t)$ , it yields

$$(\mathcal{P}_c - \mathcal{P}) \left( s(t) - \frac{1}{k} \dot{\mathcal{P}} \right) \leq 0. \quad (\text{D.2})$$

### Appendix E. Regressor and parameter vectors

The detailed expressions for the regressor vector  $\mathbf{Y}_{v31} \in \mathbb{R}^{1 \times 2}$  and the parameter vector  $\boldsymbol{\theta}_{v31} \in \mathbb{R}^2$  are written as

$$\mathbf{Y}_{v31} = \begin{bmatrix} -\frac{v(p_{s3}-p_{a3})}{x_3} S(u_{31})u_{31} \\ -\frac{v(p_{a3}-p_r)}{x_3} S(-u_{31})u_{31} \end{bmatrix}^T, \quad \boldsymbol{\theta}_{v31} = \begin{bmatrix} c_{p1} \\ c_{n1} \end{bmatrix}. \quad (\text{E.1})$$

The detailed expressions for the regressor vector  $\mathbf{Y}_{v32} \in \mathbb{R}^{1 \times 2}$  and the parameter vector  $\boldsymbol{\theta}_{v32} \in \mathbb{R}^2$  are written as

$$\mathbf{Y}_{v32} = \begin{bmatrix} -\frac{v(p_{s3}-p_{b3})}{s_3-x_3} S(u_{32})u_{32} \\ -\frac{v(p_{b3}-p_r)}{s_3-x_3} S(-u_{32})u_{32} \end{bmatrix}^T, \quad \boldsymbol{\theta}_{v32} = \begin{bmatrix} c_{p2} \\ c_{n2} \end{bmatrix}. \quad (\text{E.2})$$

The detailed expressions for the regressor vector  $\mathbf{Y}_{d31} \in \mathbb{R}^{1 \times 2}$  and the parameter vector  $\boldsymbol{\theta}_{d31} \in \mathbb{R}^2$  are written as

$$\mathbf{Y}_{d31} = \begin{bmatrix} \dot{p}_{a3r} & \frac{\dot{x}_3}{x_3} \end{bmatrix}, \quad \boldsymbol{\theta}_{d31} = \begin{bmatrix} \frac{A_{a3}}{\beta_f} & A_{a3} \end{bmatrix}^T. \quad (\text{E.3})$$

The detailed expressions for the regressor vector  $\mathbf{Y}_{d32} \in \mathbb{R}^{1 \times 2}$  and the parameter vector  $\boldsymbol{\theta}_{d32} \in \mathbb{R}^2$  are written as

$$\mathbf{Y}_{d32} = \begin{bmatrix} \dot{p}_{b3r} & -\frac{\dot{x}_3}{s_3-x_3} \end{bmatrix}, \quad \boldsymbol{\theta}_{d32} = \begin{bmatrix} \frac{A_{b3}}{\beta_f} & A_{b3} \end{bmatrix}^T. \quad (\text{E.4})$$

### Appendix F. Lemma 4 (Open Chain 5 Dynamics)

**Lemma 4** holds for open chain 5 control and with its parameter adaptations.

**Lemma 4.** Consider open chain 5 described by (15), (16), (18), (19), (21), (22) and (24), combined with the control equations (40), (41), (43), (44), (50), (51) and (53) and with the parameter adaptations (45)–(48). Let the non-negative accompanying function for open chain 5 be

$$v_{oc5} = v_{B_5} + v_{B_{51}} = \frac{1}{2} \sum_{\mathbf{A} \in \Psi_{oc5}} \left[ (\mathbf{A}V_{\mathbf{r}} - \mathbf{A}V)^T \mathbf{M}_{\mathbf{A}} (\mathbf{A}V_{\mathbf{r}} - \mathbf{A}V) + \sum_{\gamma=1}^{13} \frac{(\theta_{A\gamma} - \hat{\theta}_{A\gamma})^2}{\rho_{A\gamma}} \right] \quad (\text{F.1})$$

where set  $\Psi_{oc5}$  contains frames  $\{\mathbf{B}_5\}$  and  $\{\mathbf{B}_{51}\}$ . Then, the time derivative of (F.1) can be expressed by

$$\dot{v}_{oc5} = - \sum_{\mathbf{A} \in \Psi_{oc5}} (\mathbf{A}V_{\mathbf{r}} - \mathbf{A}V)^T \mathbf{K}_{\mathbf{A}} (\mathbf{A}V_{\mathbf{r}} - \mathbf{A}V) + (f_{c3r} - f_{c3})(\dot{x}_{3r} - \dot{x}_3) + p_{B_5} - p_{T_5}. \quad (\text{F.2})$$

**Proof.** Consider open chain 5 containing rigid links 5 and 51; see Fig. 5. In view of (A.6), by subtracting (18) from (43), and (19) from (44), it follows that

$$\begin{aligned} {}^A F_r^* - {}^A F^* &= M_A \frac{d}{dt} ({}^A V_r - {}^A V) + C_A ({}^A \omega) ({}^A V_r - {}^A V) \\ &\quad - Y_A (\theta_A - \hat{\theta}_A) + K_A ({}^A V_r - {}^A V) \end{aligned} \quad (F.3)$$

holds,  $\forall A \in \{B_5, B_{51}\}$ . Then, the skew-symmetric property of  $C_{B_5} ({}^{B_5} \omega)$  and  $C_{B_{51}} ({}^{B_{51}} \omega)$  yields

$$({}^{B_5} V_r - {}^{B_5} V)^T C_{B_5} ({}^{B_5} \omega) ({}^{B_5} V_r - {}^{B_5} V) = 0 \quad (F.4)$$

$$({}^{B_{51}} V_r - {}^{B_{51}} V)^T C_{B_{51}} ({}^{B_{51}} \omega) ({}^{B_{51}} V_r - {}^{B_{51}} V) = 0. \quad (F.5)$$

Let the non-negative accompanying function  $v_{oc5}$  for open chain 5 be defined as written in (F.1), i.e.,

$$\begin{aligned} v_{oc5} &= v_{B_5} + v_{B_{51}} \\ &= \frac{1}{2} ({}^{B_5} V_r - {}^{B_5} V)^T M_{B_5} ({}^{B_5} V_r - {}^{B_5} V) \\ &\quad + \frac{1}{2} ({}^{B_{51}} V_r - {}^{B_{51}} V)^T M_{B_{51}} ({}^{B_{51}} V_r - {}^{B_{51}} V) \\ &\quad + \frac{1}{2} \sum_{\gamma=1}^{13} \frac{(\theta_{B_{5\gamma}} - \hat{\theta}_{B_{5\gamma}})^2}{\rho_{B_{5\gamma}}} + \frac{1}{2} \sum_{\gamma=1}^{13} \frac{(\theta_{B_{51\gamma}} - \hat{\theta}_{B_{51\gamma}})^2}{\rho_{B_{51\gamma}}}. \end{aligned} \quad (F.6)$$

Then, using (46), (48), (D.2), (F.3) (with  $A = B_5$ ) and (F.4), the time derivative  $\dot{v}_{B_5}$  can be written as

$$\begin{aligned} \dot{v}_{B_5} &= ({}^{B_5} V_r - {}^{B_5} V)^T M_{B_5} \frac{d}{dt} ({}^{B_5} V_r - {}^{B_5} V) - \sum_{\gamma=1}^{13} (\theta_{B_{5\gamma}} - \hat{\theta}_{B_{5\gamma}}) \frac{\dot{\hat{\theta}}_{B_{5\gamma}}}{\rho_{B_{5\gamma}}} \\ &= -({}^{B_5} V_r - {}^{B_5} V)^T C_{B_5} ({}^{B_5} \omega) ({}^{B_5} V_r - {}^{B_5} V) \\ &\quad - ({}^{B_5} V_r - {}^{B_5} V)^T K_{B_5} ({}^{B_5} V_r - {}^{B_5} V) \\ &\quad + ({}^{B_5} V_r - {}^{B_5} V)^T Y_{B_5} (\theta_{B_5} - \hat{\theta}_{B_5}) \\ &\quad - \sum_{\gamma=1}^{13} (\theta_{B_{5\gamma}} - \hat{\theta}_{B_{5\gamma}}) \frac{\dot{\hat{\theta}}_{B_{5\gamma}}}{\rho_{B_{5\gamma}}} + ({}^{B_5} V_r - {}^{B_5} V)^T ({}^{B_5} F_r^* - {}^{B_5} F^*) \\ &= -({}^{B_5} V_r - {}^{B_5} V)^T K_{B_5} ({}^{B_5} V_r - {}^{B_5} V) \\ &\quad + ({}^{B_5} V_r - {}^{B_5} V)^T ({}^{B_5} F_r^* - {}^{B_5} F^*) \\ &\quad + \sum_{\gamma=1}^{13} \left\{ (\theta_{B_{5\gamma}} - \hat{\theta}_{B_{5\gamma}}) \left[ s_{B_{5\gamma}} - \frac{\dot{\hat{\theta}}_{B_{5\gamma}}}{\rho_{B_{5\gamma}}} \right] \right\} \\ &\leq -({}^{B_5} V_r - {}^{B_5} V)^T K_{B_5} ({}^{B_5} V_r - {}^{B_5} V) \\ &\quad + ({}^{B_5} V_r - {}^{B_5} V)^T ({}^{B_5} F_r^* - {}^{B_5} F^*). \end{aligned} \quad (F.7)$$

Identically to (F.7), using (45), (47), (D.2), (F.3) (with  $A = B_{51}$ ) and (F.5), the time derivative  $\dot{v}_{B_{51}}$  can be written as

$$\begin{aligned} \dot{v}_{B_{51}} &\leq -({}^{B_{51}} V_r - {}^{B_{51}} V)^T K_{B_{51}} ({}^{B_{51}} V_r - {}^{B_{51}} V) \\ &\quad + ({}^{B_{51}} V_r - {}^{B_{51}} V)^T ({}^{B_{51}} F_r^* - {}^{B_{51}} F^*). \end{aligned} \quad (F.8)$$

Then, using (15), (22), (24), (40), (51), (53) and (C.1), the term  $({}^{B_5} V_r - {}^{B_5} V)^T ({}^{B_5} F_r^* - {}^{B_5} F^*)$  in (F.7) can be written as

$$\begin{aligned} &({}^{B_5} V_r - {}^{B_5} V)^T ({}^{B_5} F_r^* - {}^{B_5} F^*) \\ &= ({}^{B_5} V_r - {}^{B_5} V)^T \left[ ({}^{B_5} F_r - {}^{B_5} F) - {}^{B_5} U_{B_{51}} ({}^{B_{51}} F_r - {}^{B_{51}} F) \right] \\ &= p_{B_5} - \left[ {}^{B_{51}} U_{B_5}^T ({}^{B_{51}} V_r - {}^{B_{51}} V) - {}^{B_{51}} U_{B_5}^T x_f (\dot{x}_{3r} - \dot{x}_3) \right]^T \\ &\quad \times {}^{B_5} U_{B_{51}} ({}^{B_{51}} F_r - {}^{B_{51}} F) \\ &= p_{B_5} - p_{B_{51}} + (\dot{x}_{3r} - \dot{x}_3) x_f^T ({}^{B_{51}} F_r - {}^{B_{51}} F) \\ &= p_{B_5} - p_{B_{51}} + (\dot{x}_{3r} - \dot{x}_3) (f_{c3r} - f_{c3}) \end{aligned} \quad (F.9)$$

and, similarly to (F.9), using (16), (21), (41), (50), and (C.1) the term  $({}^{B_{51}} V_r - {}^{B_{51}} V)^T ({}^{B_{51}} F_r^* - {}^{B_{51}} F^*)$  in (F.8) can be written as

$$\begin{aligned} &({}^{B_{51}} V_r - {}^{B_{51}} V)^T ({}^{B_{51}} F_r^* - {}^{B_{51}} F^*) \\ &= ({}^{B_{51}} V_r - {}^{B_{51}} V)^T \left[ ({}^{B_{51}} F_r - {}^{B_{51}} F) - {}^{B_{51}} U_{T_5} ({}^{T_5} F_r - {}^{T_5} F) \right] \end{aligned}$$

$$\begin{aligned} &= p_{B_{51}} - \left[ {}^{T_5} U_{B_{51}}^T ({}^{T_5} V_r - {}^{T_5} V) \right]^T {}^{B_{51}} U_{T_5} ({}^{T_5} F_r - {}^{T_5} F) \\ &= p_{B_{51}} - p_{T_5}. \end{aligned} \quad (F.10)$$

Finally, taking the time derivative from (F.1), and using (F.7)–(F.10) yields

$$\begin{aligned} \dot{v}_{oc5} &= \dot{v}_{B_5} + \dot{v}_{B_{51}} \\ &\leq - \sum_{A \in \mathcal{V}_{oc5}} ({}^A V_r - {}^A V)^T K_A ({}^A V_r - {}^A V) \\ &\quad + (f_{c3r} - f_{c3}) (\dot{x}_{3r} - \dot{x}_3) + p_{B_5} - p_{T_5} \end{aligned} \quad (F.11)$$

where set  $\mathcal{V}_{oc5}$  contains frames  $\{B_5\}$  and  $\{B_{51}\}$ , qualifying the proof for Lemma 4. ■

## Appendix G. Lemma 5 (Chamber A Dynamics)

Lemma 5 holds for chamber A control with its parameter adaptations.

**Lemma 5.** Consider the hydraulic cylinder chamber A dynamics described by (32) and (34), combined with the respective control equations (57) and (59), and with the parameter adaptation (60)–(63). Let the non-negative accompanying function for this subsystem be

$$\begin{aligned} v_{a3} &= \frac{A_{a3}^2}{2\beta_f k_{x31}} (p_{a3r} - p_{a3})^2 + \frac{A_{a3}}{2k_{x31}} \sum_{\gamma=1}^2 \frac{(\theta_{d31\gamma} - \hat{\theta}_{d31\gamma})^2}{\rho_{d31\gamma}} \\ &\quad + \frac{A_{a3}}{2k_{x31}} \sum_{\gamma=1}^2 \frac{(\theta_{v31\gamma} - \hat{\theta}_{v31\gamma})^2}{\rho_{v31\gamma}}. \end{aligned} \quad (G.1)$$

Then, the time derivative of (G.1) can be expressed by

$$\dot{v}_{a3} \leq - \frac{A_{a3} k_{p31}}{k_{x31}} (p_{a3r} - p_{a3})^2 - A_{a3} (p_{a3r} - p_{a3}) (\dot{x}_{3r} - \dot{x}_3). \quad (G.2)$$

**Proof.** It follows from (32), (34), (57), and (59) that

$$\begin{aligned} \frac{A_{a3}}{\beta} (\dot{p}_{a3r} - \dot{p}_{a3}) &= Y_{v31} (\theta_{v31} - \hat{\theta}_{v31}) + Y_{d31} (\theta_{d31} - \hat{\theta}_{d31}) \\ &\quad - k_{p31} (p_{a3r} - p_{a3}) - k_{x31} (\dot{x}_{3r} - \dot{x}_3) \end{aligned} \quad (G.3)$$

holds. Differentiating  $v_{a3}$  in (G.1) with respect to time and using (60), (61), (D.2) and (G.3) yields

$$\begin{aligned} \dot{v}_{a3} &= (p_{a3r} - p_{a3}) \frac{A_{a3}^2}{\beta_f k_{x31}} (\dot{p}_{a3r} - \dot{p}_{a3}) \\ &\quad - \frac{A_{a3}}{k_{x31}} \sum_{\gamma=1}^2 \left[ (\theta_{d31\gamma} - \hat{\theta}_{d31\gamma}) \frac{\dot{\hat{\theta}}_{d31\gamma}}{\rho_{d31\gamma}} + (\theta_{v31\gamma} - \hat{\theta}_{v31\gamma}) \frac{\dot{\hat{\theta}}_{v31\gamma}}{\rho_{v31\gamma}} \right] \\ &= - \frac{A_{a3} k_{p31}}{k_{x31}} (p_{a3r} - p_{a3})^2 - A_{a3} (p_{a3r} - p_{a3}) (\dot{x}_{3r} - \dot{x}_3) \\ &\quad + \frac{A_{a3}}{k_{x31}} \left[ (p_{a3r} - p_{a3}) Y_{d31} (\theta_{d31} - \hat{\theta}_{d31}) - \sum_{\gamma=1}^2 (\theta_{d31\gamma} - \hat{\theta}_{d31\gamma}) \frac{\dot{\hat{\theta}}_{d31\gamma}}{\rho_{d31\gamma}} \right. \\ &\quad \left. + (p_{a3r} - p_{a3}) Y_{v31} (\theta_{v31} - \hat{\theta}_{v31}) - \sum_{\gamma=1}^2 (\theta_{v31\gamma} - \hat{\theta}_{v31\gamma}) \frac{\dot{\hat{\theta}}_{v31\gamma}}{\rho_{v31\gamma}} \right] \\ &= - \frac{A_{a3} k_{p31}}{k_{x31}} (p_{a3r} - p_{a3})^2 - A_{a3} (p_{a3r} - p_{a3}) (\dot{x}_{3r} - \dot{x}_3) \\ &\quad + \frac{A_{a3}}{k_{x31}} \sum_{\gamma=1}^2 (\theta_{d31\gamma} - \hat{\theta}_{d31\gamma}) \left( s_{d31\gamma} - \frac{\dot{\hat{\theta}}_{d31\gamma}}{\rho_{d31\gamma}} \right) \\ &\quad + \frac{A_{a3}}{k_{x31}} \sum_{\gamma=1}^2 (\theta_{v31\gamma} - \hat{\theta}_{v31\gamma}) \left( s_{v31\gamma} - \frac{\dot{\hat{\theta}}_{v31\gamma}}{\rho_{v31\gamma}} \right) \\ &\leq - \frac{A_{a3} k_{p31}}{k_{x31}} (p_{a3r} - p_{a3})^2 - A_{a3} (p_{a3r} - p_{a3}) (\dot{x}_{3r} - \dot{x}_3) \end{aligned} \quad (G.4)$$

which qualifies the proof for Lemma 5. ■

## Appendix H. Lemma 6 (Chamber B Dynamics)

Lemma 6 holds for chamber B control with its parameter adaptations.

**Lemma 6.** Consider the hydraulic cylinder chamber B dynamics described by (33) and (35), combined with the respective control equations (64) and (66), and with the parameter adaptation (67)–(70). Let the non-negative accompanying function for this subsystem be

$$v_{b3} = \frac{A_{b3}^2}{2\beta_f k_{x32}} (p_{b3r} - p_{b3})^2 + \frac{A_{b3}}{2k_{x32}} \sum_{\gamma=1}^2 \frac{(\theta_{d32\gamma} - \hat{\theta}_{d32\gamma})^2}{\rho_{d32\gamma}} + \frac{A_{b3}}{2k_{x32}} \sum_{\gamma=1}^2 \frac{(\theta_{v32\gamma} - \hat{\theta}_{v32\gamma})^2}{\rho_{v32\gamma}}. \quad (H.1)$$

Then, the time derivative of (H.1) can be expressed by

$$\dot{v}_{b3} \leq -\frac{A_{b3} k_{p32}}{k_{x32}} (p_{b3r} - p_{b3})^2 + A_{b3} (p_{b3r} - p_{b3}) (\dot{x}_{3r} - \dot{x}_3). \quad (H.2)$$

**Proof.** It follows from (33), (35), (64), and (66) that

$$\frac{A_{b3}}{\beta} (\dot{p}_{b3r} - \dot{p}_{b3}) = Y_{v32} (\theta_{v32} - \hat{\theta}_{v32}) + Y_{d32} (\theta_{d32} - \hat{\theta}_{d32}) - k_{p32} (p_{b3r} - p_{b3}) + k_{x32} (\dot{x}_{3r} - \dot{x}_3) \quad (H.3)$$

holds. Differentiating  $v_{b3}$  in (H.1) with respect to time and using (67), (68), (D.2) and (H.3) yields

$$\begin{aligned} \dot{v}_{b3} &= (p_{b3r} - p_{b3}) \frac{A_{b3}}{\beta_f k_{x32}} (\dot{p}_{b3r} - \dot{p}_{b3}) \\ &\quad - \frac{A_{b3}}{k_{x32}} \sum_{\gamma=1}^2 \left[ (\theta_{d32\gamma} - \hat{\theta}_{d32\gamma}) \frac{\dot{\hat{\theta}}_{d32\gamma}}{\rho_{d32\gamma}} + (\theta_{v32\gamma} - \hat{\theta}_{v32\gamma}) \frac{\dot{\hat{\theta}}_{v32\gamma}}{\rho_{v32\gamma}} \right] \\ &= -\frac{A_{b3} k_{p32}}{k_{x32}} (p_{b3r} - p_{b3})^2 + A_{b3} (p_{b3r} - p_{b3}) (\dot{x}_{3r} - \dot{x}_3) \\ &\quad + \frac{A_{b3}}{k_{x32}} \left[ (p_{b3r} - p_{b3}) Y_{d32} (\theta_{d32} - \hat{\theta}_{d32}) - \sum_{\gamma=1}^2 (\theta_{d32\gamma} - \hat{\theta}_{d32\gamma}) \frac{\dot{\hat{\theta}}_{d32\gamma}}{\rho_{d32\gamma}} \right. \\ &\quad \left. + (p_{b3r} - p_{b3}) Y_{v32} (\theta_{v32} - \hat{\theta}_{v32}) - \sum_{\gamma=1}^2 (\theta_{v32\gamma} - \hat{\theta}_{v32\gamma}) \frac{\dot{\hat{\theta}}_{v32\gamma}}{\rho_{v32\gamma}} \right] \\ &= -\frac{A_{b3} k_{p32}}{k_{x32}} (p_{b3r} - p_{b3})^2 + A_{b3} (p_{b3r} - p_{b3}) (\dot{x}_{3r} - \dot{x}_3) \\ &\quad + \frac{A_{b3}}{k_{x32}} \sum_{\gamma=1}^2 (\theta_{d32\gamma} - \hat{\theta}_{d32\gamma}) \left( s_{d32\gamma} - \frac{\dot{\hat{\theta}}_{d32\gamma}}{\rho_{d32\gamma}} \right) \\ &\quad + \frac{A_{b3}}{k_{x32}} \sum_{\gamma=1}^2 (\theta_{v32\gamma} - \hat{\theta}_{v32\gamma}) \left( s_{v32\gamma} - \frac{\dot{\hat{\theta}}_{v32\gamma}}{\rho_{v32\gamma}} \right) \\ &\leq -\frac{A_{b3} k_{p32}}{k_{x32}} (p_{b3r} - p_{b3})^2 + A_{b3} (p_{b3r} - p_{b3}) (\dot{x}_{3r} - \dot{x}_3) \end{aligned} \quad (H.4)$$

which qualifies the proof for Lemma 6. ■

## Appendix I. Lemma 7 (Hydraulic Cylinder Dynamics)

Lemma 7 holds for the control of the hydraulic cylinder dynamics with its parameter adaptation.

**Lemma 7.** Consider the hydraulic cylinder dynamics, decomposed to chambers A and B dynamics in Lemmas 5 and 6, and with the piston dynamics described by (25)–(27), combined with the control laws (54) and (71), and with the parameter adaptation (55) and (56). Let the non-negative accompanying function for the hydraulic cylinder be

$$v_{c3} = v_{a3} + v_{b3} + \frac{1}{2} \sum_{\gamma=1}^7 \frac{(\theta_{f3\gamma} - \hat{\theta}_{f3\gamma})^2}{\rho_{f3\gamma}}$$

$$\begin{aligned} &= \frac{A_{a3}^2}{2\beta_f k_{x31}} (p_{a3r} - p_{a3})^2 + \frac{A_{b3}^2}{2\beta_f k_{x32}} (p_{b3r} - p_{b3})^2 \\ &\quad + \frac{A_{a3}}{2k_{x31}} \sum_{\gamma=1}^2 \left[ \frac{(\theta_{d31\gamma} - \hat{\theta}_{d31\gamma})^2}{\rho_{d31\gamma}} + \frac{(\theta_{v31\gamma} - \hat{\theta}_{v31\gamma})^2}{\rho_{v31\gamma}} \right] \\ &\quad + \frac{A_{b3}}{2k_{x32}} \sum_{\gamma=1}^2 \left[ \frac{(\theta_{d32\gamma} - \hat{\theta}_{d32\gamma})^2}{\rho_{d32\gamma}} + \frac{(\theta_{v32\gamma} - \hat{\theta}_{v32\gamma})^2}{\rho_{v32\gamma}} \right] \\ &\quad + \frac{1}{2} \sum_{\gamma=1}^7 \frac{(\theta_{f3\gamma} - \hat{\theta}_{f3\gamma})^2}{\rho_{f3\gamma}}. \end{aligned} \quad (I.1)$$

Then, the time derivative of (I.1) can be expressed by

$$\dot{v}_{c3} \leq -\frac{A_{a3} k_{p31}}{k_{x31}} (p_{a3r} - p_{a3})^2 - \frac{A_{b3} k_{p32}}{k_{x32}} (p_{b3r} - p_{b3})^2 - (f_{c3r} - f_{c3}) (\dot{x}_{3r} - \dot{x}_3). \quad (I.2)$$

**Proof.** Differentiating  $v_{c3}$  in (I.1) with respect to time and using (25)–(27), (54)–(56), (71), (D.2), (G.2), and (H.2) yields

$$\begin{aligned} \dot{v}_{c3} &= \dot{v}_{a3} + \dot{v}_{b3} - \sum_{\gamma=1}^7 (\theta_{f3\gamma} - \hat{\theta}_{f3\gamma}) \frac{\dot{\hat{\theta}}_{f3\gamma}}{\rho_{f3\gamma}} \\ &\leq -\frac{A_{a3} k_{p31}}{k_{x31}} (p_{a3r} - p_{a3})^2 - A_{a3} (p_{a3r} - p_{a3}) (\dot{x}_{3r} - \dot{x}_3) \\ &\quad - \frac{A_{b3} k_{p32}}{k_{x32}} (p_{b3r} - p_{b3})^2 + A_{b3} (p_{b3r} - p_{b3}) (\dot{x}_{3r} - \dot{x}_3) \\ &\quad - \sum_{\gamma=1}^7 (\theta_{f3\gamma} - \hat{\theta}_{f3\gamma}) \frac{\dot{\hat{\theta}}_{f3\gamma}}{\rho_{f3\gamma}} \\ &= -\frac{A_{a3} k_{p31}}{k_{x31}} (p_{a3r} - p_{a3})^2 - \frac{A_{b3} k_{p32}}{k_{x32}} (p_{b3r} - p_{b3})^2 \\ &\quad - (f_{p3r} - f_{p3}) (\dot{x}_{3r} - \dot{x}_3) - \sum_{\gamma=1}^7 (\theta_{f3\gamma} - \hat{\theta}_{f3\gamma}) \frac{\dot{\hat{\theta}}_{f3\gamma}}{\rho_{f3\gamma}} \\ &= -\frac{A_{a3} k_{p31}}{k_{x31}} (p_{a3r} - p_{a3})^2 - \frac{A_{b3} k_{p32}}{k_{x32}} (p_{b3r} - p_{b3})^2 \\ &\quad + (\dot{x}_{3r} - \dot{x}_3) Y_{f3} (\theta_{f3} - \hat{\theta}_{f3}) - \sum_{\gamma=1}^7 (\theta_{f3\gamma} - \hat{\theta}_{f3\gamma}) \frac{\dot{\hat{\theta}}_{f3\gamma}}{\rho_{f3\gamma}} \\ &\quad - (f_{c3r} - f_{c3}) (\dot{x}_{3r} - \dot{x}_3) \\ &= -\frac{A_{a3} k_{p31}}{k_{x31}} (p_{a3r} - p_{a3})^2 - \frac{A_{b3} k_{p32}}{k_{x32}} (p_{b3r} - p_{b3})^2 \\ &\quad - (f_{c3r} - f_{c3}) (\dot{x}_{3r} - \dot{x}_3) + \sum_{\gamma=1}^7 (\theta_{f3\gamma} - \hat{\theta}_{f3\gamma}) \left( s_{f3\gamma} - \frac{\dot{\hat{\theta}}_{f3\gamma}}{\rho_{f3\gamma}} \right) \\ &\leq -\frac{A_{a3} k_{p31}}{k_{x31}} (p_{a3r} - p_{a3})^2 - \frac{A_{b3} k_{p32}}{k_{x32}} (p_{b3r} - p_{b3})^2 \\ &\quad - (f_{c3r} - f_{c3}) (\dot{x}_{3r} - \dot{x}_3) \end{aligned} \quad (I.3)$$

which qualifies the proof for Lemma 7. ■

## Appendix J. Proof for Theorem 1

The proof for Theorem 1 follows directly from Lemmas 4 and 7. Using (F.1) and (I.1), the non-negative accompanying function  $v_5$  can be written as

$$\begin{aligned} v_5 &= v_{oc5} + v_{c3} \\ &= \frac{1}{2} \sum_{A \in \mathcal{V}_{oc5}} (A V_r - A V)^T M_A (A V_r - A V) \\ &\quad + \frac{1}{2} \sum_{\gamma=1}^{13} \left[ \frac{(\theta_{B5\gamma} - \hat{\theta}_{B5\gamma})^2}{\rho_{B5\gamma}} + \frac{(\theta_{B51\gamma} - \hat{\theta}_{B51\gamma})^2}{\rho_{B51\gamma}} \right] \end{aligned}$$



$$\begin{aligned}
& + \frac{A_{a3}^2}{2\beta_f k_{x31}} (p_{a3r} - p_{a3})^2 + \frac{A_{b3}^2}{2\beta_f k_{x32}} (p_{b3r} - p_{b3})^2 \\
& + \frac{A_{a3}}{2k_{x31}} \sum_{\gamma=1}^2 \left[ \frac{(\theta_{d31\gamma} - \hat{\theta}_{d31\gamma})^2}{\rho_{d31\gamma}} + \frac{(\theta_{v31\gamma} - \hat{\theta}_{v31\gamma})^2}{\rho_{v31\gamma}} \right] \\
& + \frac{A_{b3}}{2k_{x32}} \sum_{\gamma=1}^2 \left[ \frac{(\theta_{d32\gamma} - \hat{\theta}_{d32\gamma})^2}{\rho_{d32\gamma}} + \frac{(\theta_{v32\gamma} - \hat{\theta}_{v32\gamma})^2}{\rho_{v32\gamma}} \right] \\
& + \frac{1}{2} \sum_{\gamma=1}^7 \frac{(\theta_{f3\gamma} - \hat{\theta}_{f3\gamma})^2}{\rho_{f3\gamma}} \\
& \geq \frac{1}{2} \sum_{A \in \Psi_{oc5}} (A V_r - A V)^T M_A (A V_r - A V) \\
& + \frac{A_{a3}^2}{2\beta_f k_{x31}} (p_{a3r} - p_{a3})^2 + \frac{A_{b3}^2}{2\beta_f k_{x32}} (p_{b3r} - p_{b3})^2. \tag{J.1}
\end{aligned}$$

Then, it follows from (F.2) and (I.2) that the time derivative  $\dot{v}_5$  can be written as

$$\begin{aligned}
\dot{v}_5 &= \dot{v}_{oc5} + \dot{v}_{c3} \\
&\leq - \sum_{A \in \Psi_{oc5}} (A V_r - A V)^T K_A (A V_r - A V) + p_{B_5} - p_{T_5} \\
&\quad - \frac{A_{a3} k_{p31}}{k_{x31}} (p_{a3r} - p_{a3})^2 - \frac{A_{b3} k_{p32}}{k_{x32}} (p_{b3r} - p_{b3})^2 \\
&\quad + (f_{c3r} - f_{c3})(\dot{x}_{3r} - \dot{x}_3) - (f_{c3r} - f_{c3})(\dot{x}_{3r} - \dot{x}_3) \\
&= - \sum_{A \in \Psi_{oc5}} (A V_r - A V)^T K_A (A V_r - A V) + p_{B_5} - p_{T_5} \\
&\quad - \frac{A_{a3} k_{p31}}{k_{x31}} (p_{a3r} - p_{a3})^2 - \frac{A_{b3} k_{p32}}{k_{x32}} (p_{b3r} - p_{b3})^2. \tag{J.2}
\end{aligned}$$

Consider that the subsystem has one *driven* VCP and one *driving* VCP associated with frames  $\{B_5\}$  and  $\{T_5\}$ , respectively. Then, (J.1) and (J.2) complete the proof of the virtual stability of the subsystem in the sense of Definition 3. ■

## Appendix K. Proof for Theorem 4

The proof for Theorem 4 follows directly from Theorems 1–3. It follows from (72), (74) and (76) that

$$\begin{aligned}
v_{tot} &= v_R + v_5 + v_{O_3} \\
&\geq \frac{1}{2} \sum_{A \in \Phi} (A V_r - A V)^T M_A (A V_r - A V) \\
&\quad + \frac{1}{2} \sum_{i=1}^3 \left[ \frac{A_{ai}^2}{\beta_f k_{xi1}} (p_{air} - p_{ai})^2 + \frac{A_{bi}^2}{\beta_f k_{xi2}} (p_{bir} - p_{bi})^2 \right] \tag{K.1}
\end{aligned}$$

holds, where set  $\Phi$  contains frame  $\{O_3\}$  and sets  $\Psi_{oc5}$  and  $\Psi_r$ . Then, using (73), (75) and (77)–(80), it yields

$$\begin{aligned}
\dot{v}_{tot} &= \dot{v}_R + \dot{v}_5 + \dot{v}_{O_3} \\
&\leq - \sum_{A \in \Phi} (A V_r - A V)^T K_A (A V_r - A V) \\
&\quad - \sum_{i=1}^3 \left[ \frac{A_{ai} k_{pi1}}{k_{xi1}} (p_{air} - p_{ai})^2 + \frac{A_{bi} k_{pi2}}{k_{xi2}} (p_{bir} - p_{bi})^2 \right] \\
&\quad + \underbrace{p_{T_{O3}} - p_{T_5} + p_{B_5} - p_{B_{O2}} - p_G}_{=0, \text{ in view of (78)–(80)}} \tag{K.2}
\end{aligned}$$

It follows from Lemma 1 in Appendix B, (K.1), and (K.2) that  $(A V_r - A V) \in L_2 \cap L_\infty$ ,  $\forall A \in \Phi$ ,  $(p_{air} - p_{ai}) \in L_2 \cap L_\infty$  and  $(p_{bir} - p_{bi}) \in L_2 \cap L_\infty$ ,  $\forall i \in \{1, 2, 3\}$  hold. Then, using (15), (40) and  $(A V_r - A V) \in L_2 \cap L_\infty$ , it yields  $(\dot{x}_{ir} - \dot{x}_i) \in L_2 \cap L_\infty$ . Finally, subtracting  $\dot{x}_i$  from both sides of (38), and using  $(\dot{x}_{ir} - \dot{x}_i) \in L_2 \cap L_\infty$  and Lemma 2 (in Appendix B), it yields that  $(\dot{x}_{id} - \dot{x}_i) \in L_2 \cap L_\infty$  and  $(x_{id} - x_i) \in L_2 \cap L_\infty$  hold. ■

## References

- Alleyne, A., & Liu, R. (1999). On the limitations of force tracking control for hydraulic servosystems. *Journal of Dynamic Systems, Measurement, and Control*, 121(2), 184–190.
- Bech, M. M., Andersen, T. O., Pedersen, H. C., & Schmidt, L. (2013). Experimental evaluation of control strategies for hydraulic servo robot. In *Proc. of IEEE int. conf. on mechat. and autom. (ICMA)* (pp. 342–347).
- Boaventura, T., Buchli, J., Semini, C., & Caldwell, D. G. (2015). Model-based hydraulic impedance control for dynamic robots. *IEEE Transactions on Robotics*, 31(6), 1324–1336.
- Bonsignorio, F., & del Pobil, A. P. (2015). Toward replicable and measurable robotics research [from the guest editors]. *IEEE Robotics & Automation Magazine*, 22(3), 32–32.
- Choi, K., Seo, J., Nam, Y., & Kim, K. U. (2015). Energy-saving in excavators with application of independent metering valve. *Journal of Mechanical Science and Technology*, 29(1), 387–395.
- Daily, M., Medasani, S., Behringer, R., & Trivedi, M. (2017). Self-driving cars. *Computer*, 50(12), 18–23.
- Edge, K. A. (1997). The control of fluid power systems — responding to the challenges. *Proceedings of the Institution of Mechanical Engineers, Part I: Journal of Systems and Control Engineering*, 211(2), 91–110.
- Eriksson, B., & Palmberg, J.-O. (2011). Individual metering fluid power systems: challenges and opportunities. *Proceedings of the Institution of Mechanical Engineers, Part I: Journal of Systems and Control Engineering*, 225(2), 196–211.
- EU Robotics (2014). Strategic research agenda for robotics in europe 2014–2020. URL: [https://eu-robotics.net/cms/upload/topic\\_groups/SRA2020\\_SPARC.pdf](https://eu-robotics.net/cms/upload/topic_groups/SRA2020_SPARC.pdf). (Accessed 28 June 2017).
- European Commission (2012). Energy efficiency directive. URL: <http://eur-lex.europa.eu/legal-content/EN/TXT/?uri=CELEX:32012L0027>. (Accessed 9 June 2017).
- Government of China (2017). The 13th five-year plan for economic and social development of the people's republic of China (2016–2020). URL: <http://en.ndrc.gov.cn/newsrelease/201612/P020161207645765233498.pdf>. (Accessed 9 June 2017).
- Grabbel, J., & Ivantysynova, M. (2005). An investigation of swash plate control concepts for displacement controlled actuators. *International Journal of Fluid Power*, 6(2), 19–36.
- Gribbins, K. (2016). Compact equipment: The ultimate 2016 compact excavator market watch. URL: <http://compactequip.com/excavators/the-2016-compact-excavator-market-watch/>. (Accessed 8 Aug. 2017).
- HIAB (2017). Crane tip control. URL: [www.hiab.com/en/company/newsroom/news/hiab-crane-tip-control/](http://www.hiab.com/en/company/newsroom/news/hiab-crane-tip-control/). (Accessed 25 June 2017).
- Hippalgaonkar, R., & Ivantysynova, M. (2016). Optimal power management for DC hydraulic hybrid multi-actuator machines — Parts I–II. *Journal of Dynamic Systems, Measurement, and Control*, 138(5).
- Huova, M., Karvonen, M., Ahola, V., Linjama, M., & Vilenius, M. (2010). Energy efficient control of multiactuator digital hydraulic mobile machine. In *7th international fluid power conference*.
- Hutter, M., Leemann, P., Hottiger, G., Figi, R., Tagmann, S., Rey, G., et al. (2017). Force control for active chassis balancing. *IEEE/ASME Transactions on Mechatronics*, 22(2), 613–622.
- Hyon, S. H., Suwaka, D., Torii, Y., & Oku, N. (2017a). Design and experimental evaluation of a fast torque-controlled hydraulic humanoid robot. *IEEE/ASME Transactions on Mechatronics*, 22(2), 623–634.
- Hyon, S.-H., Tanimoto, S., & Asao, S. (2017b). Toward compliant, fast, high-precision, and low-cost manipulator with hydraulic hybrid servo booster. In *Proc. of int. conf. on robotics and autom. (ICRA)* (pp. 39–44).
- International Federation of Robotics (IFR) (2017). Executive summary world robotics 2016 industrial robots. URL: [https://ifr.org/img/uploads/Executive\\_Summary\\_WRI\\_Industrial\\_Robots\\_20161.pdf](https://ifr.org/img/uploads/Executive_Summary_WRI_Industrial_Robots_20161.pdf). (Accessed 28 June 2017).
- Jansson, A., & Palmberg, J.-O. (1990). Separate controls of meter-in and meter-out orifices in mobile hydraulic systems. SAE Technical Paper.
- John Deere (2013). News releases. URL: [www.deere.com/en\\_US/corporate/our\\_company/news\\_and\\_media/press\\_releases/2013/forestry/2013oct17\\_intelligent\\_boom\\_control.page](http://www.deere.com/en_US/corporate/our_company/news_and_media/press_releases/2013/forestry/2013oct17_intelligent_boom_control.page). (Accessed 25 June 2017).
- Johnson, J. L. (1995). *Design of electrohydraulic systems for industrial motion control* (2nd Ed.). Parker Hannifin Corporation.
- Karvonen, M. (2016). *Energy efficient digital hydraulic power management of a multi actuator system* (Ph.D. thesis), Tampere, Finland: Tampere University of Technology.
- Koivumäki, J., Honkakorpi, J., Vihonen, J., & Mattila, J. (2014). Hydraulic manipulator virtual decomposition control with performance analysis using low-cost MEMS sensors. In *Proc. IEEE/ASME int. conf. adv. intell. mechatronics* (pp. 910–917).
- Koivumäki, J., & Mattila, J. (2013). An energy-efficient high performance motion control of a hydraulic crane applying virtual decomposition control. In *Proc. IEEE/RJS int. conf. intell. robots syst. (IROS)* (pp. 4426–4433).
- Koivumäki, J., & Mattila, J. (2015a). High performance non-linear motion/force controller design for redundant hydraulic construction crane automation. *Automation in Construction*, 51, 59–77.
- Koivumäki, J., & Mattila, J. (2015b). Stability-guaranteed force-sensorless contact force/motion control of heavy-duty hydraulic manipulators. *IEEE Transactions on Robotics*, 31(4), 918–935.
- Koivumäki, J., & Mattila, J. (2017a). Stability-guaranteed impedance control of hydraulic robotic manipulators. *IEEE/ASME Transactions on Mechatronics*, 22(2), 601–612.

- Koivumäki, J., & Mattila, J. (2017b). Adaptive and nonlinear control of discharge pressure for variable displacement axial piston pumps. *ASME Journal of Dynamic Systems, Measurement, and Control*, 139(10).
- Koivumäki, J., & Mattila, J. (2017c). Adaptive and nonlinear model-based control of variable displacement pumps for variable loading conditions. In *Proc. of IEEE conf. on control techn. and applications (CCTA)* (pp. 1967–1974).
- Koivumäki, J., Mattila, J., Semini, C., & Caldwell, D. G. (2017). Stability-guaranteed nonlinear model-based control of hydraulically actuated lightweight structures. In *ASME/BATH symp. on fluid power and motion control*.
- Krstić, M., Kanellakopoulos, I., & Kokotović, P. (1995). *Nonlinear and adaptive control design*. John Wiley & Sons, Inc.
- Kuindersma, S., Deits, R., Fallon, M., Valenzuela, A., Dai, H., Permenter, F., . . . , & Tedrake, R. (2016). Optimization-based locomotion planning, estimation, and control design for the atlas humanoid robot. *Autonomous Robots*, 40(3), 429–455.
- Linjama, M. (2011). Digital fluid power: State of the art. In *12th Scandinavian int. conf. on fluid power* (pp. 331–353).
- Liu, K., Gao, Y., Tu, Z., & Lin, P. (2016). Energy-saving analysis of the independent metering system with pressure compensation for excavator's manipulator. *Proceedings of the Institution of Mechanical Engineers, Part I: Journal of Systems and Control Engineering*, 230(9), 905–920.
- Liu, S., & Yao, B. (2008). Coordinate control of energy saving programmable valves. *IEEE Transactions on Control Systems and Technology*, 16(1), 34–45.
- Lovrec, D., & Ulaga, S. (2007). Pressure control in hydraulic systems with variable or constant pumps? *Experimental Techniques*, 31(2), 33–41.
- Lu, L., & Yao, B. (2014). Energy-saving adaptive robust control of a hydraulic manipulator using five cartridge valves with an accumulator. *IEEE Transactions on Industrial Electronics*, 61(12), 7046–7054.
- Lübbert, J., Sitte, A., & Weber, J. (2016). Pressure compensator control—a novel independent metering architecture. In *10th international fluid power conference* (pp. 231–246).
- Mattila, J., Koivumäki, J., Caldwell, D. G., & Semini, C. (2017). A survey on control of hydraulic robotic manipulators with projection to future trends. *IEEE/ASME Transactions on Mechatronics*, 22(2), 669–680.
- Mattila, J., & Virvalo, T. (2000). Energy-efficient motion control of a hydraulic manipulator. In *IEEE int. conf. on robotics and autom. (ICRA)*, vol. 3 (pp. 3000–3006).
- Mistry, M., Buchli, J., & Schaal, S. (2010). Inverse dynamics control of floating base systems using orthogonal decomposition. In *Proc. of the IEEE int. conf. on robotics and automation (ICRA)* (pp. 3406–3412).
- MOOG (2015). Moog E024 series servo valve datasheet. URL: [www.moog.com/literature/ICD/moog\\_e024\\_technical\\_brochure.pdf](http://www.moog.com/literature/ICD/moog_e024_technical_brochure.pdf). (Accessed 22 July 2017).
- Nurmi, J., & Mattila, J. (2017). Global energy-optimal redundancy resolution of hydraulic manipulators: Experimental results for a forestry manipulator. *Energies*, 10(5), 647.
- Parker Hannifin (2016). Variable displacement axial piston pumps, Series P2/P3, datasheet. URL: [www.parker.com/literature/PMDE/Catalogs/Piston\\_Pumps/P2-P3/HY30-2800-UK.pdf](http://www.parker.com/literature/PMDE/Catalogs/Piston_Pumps/P2-P3/HY30-2800-UK.pdf). (Accessed 22 July 2017).
- Rong, X., Li, Y., Ruan, J., & Li, B. (2012). Design and simulation for a hydraulic actuated quadruped robot. *Journal of Mechanical Science and Technology*, 26(4), 1171–1177.
- Semini, C., Barasuol, V., Boaventura, T., Frigerio, M., Focchi, M., Caldwell, D. G., et al. (2015). Towards versatile legged robots through active impedance control. *International Journal of Robotics Research*, 34(7), 1003–1020.
- Semini, C., Barasuol, V., Goldsmith, J., Frigerio, M., Focchi, M., Gao, Y., et al. (2017). Design of the hydraulically actuated, torque-controlled quadruped robot HyQ2Max. *IEEE/ASME Transactions on Mechatronics*, 22(2), 635–646.
- Seok, S., Wang, A., Chuah, M. Y. M., Hyun, D. J., Lee, J., Otten, D. M., . . . , & Kim, S. (2015). Design principles for energy-efficient legged locomotion and implementation on the MIT cheetah robot. *IEEE/ASME Transactions on Mechatronics*, 20(3), 1117–1129.
- Slotine, J.-J. E., & Li, W. (1991). *Applied nonlinear control*. Englewood Cliffs, NJ: Prentice-Hall.
- Tao, G. (1997). A simple alternative to the Barbalat lemma. *IEEE Transactions on Automatic Control*, 42(5).
- Vukovic, M., Leifeld, R., & Murrenhoff, H. (2017). Reducing fuel consumption in hydraulic excavators — a comprehensive analysis. *Energies*, 10(5), 687.
- Watton, J. (1989). *Fluid power systems: modelling, simulation, analog and microcomputer control*. New York: Prentice Hall.
- Xi, W., Yesilevskiy, Y., & Remy, C. D. (2016). Selecting gaits for economical locomotion of legged robots. *International Journal of Robotics Research*, 35(9), 1140–1154.
- Xu, B., Ding, R., Zhang, J., Cheng, M., & Sun, T. (2015). Pump/valves coordinate control of the independent metering system for mobile machinery. *Automation in Construction*, 57, 98–111.
- Yao, B., Bu, F., & Chiu, G. (2001). Non-linear adaptive robust control of electro-hydraulic systems driven by double-rod actuators. *International Journal of Control*, 74(8), 761–775.
- Yao, J., Deng, W., & Jiao, Z. (2015). Adaptive control of hydraulic actuators with lugre model-based friction compensation. *IEEE Transactions on Industrial Electronics*, 62(10), 6469–6477.
- Yao, J., Jiao, Z., Ma, D., & Yan, L. (2014). High-accuracy tracking control of hydraulic rotary actuators with modeling uncertainties. *IEEE/ASME Transactions on Mechatronics*, 19(2), 633–641.
- Zhu, W.-H. (2010). *Virtual decomposition control — toward hyper degrees of freedom robots*. Springer-Verlag.
- Zhu, Wen-Hong (2014). FPGA logic devices for precision control: An application to large friction actuators with payloads. *IEEE Control Systems*, 34(3), 54–75.
- Zhu, W.-H., Bien, Z., & De Schutter, J. (1998). Adaptive motion/force control of multiple manipulators with joint flexibility based on virtual decomposition. *IEEE Transactions on Automatic Control*, 43(1), 46–60.
- Zhu, W.-H., & De Schutter, J. (1999a). Adaptive control of mixed rigid/flexible joint robot manipulators based on virtual decomposition. *IEEE Transactions on Robotics and Automation*, 15(2), 310–317.
- Zhu, W.-H., & De Schutter, J. (1999b). Control of two industrial manipulators rigidly holding an egg. *IEEE Control Systems Magazine*, 19(2), 24–30.
- Zhu, W.-H., & De Schutter, J. (2002). Experimental verifications of virtual-decomposition-based motion/force control. *IEEE Transactions on Robotics and Automation*, 18(3), 379–386.
- Zhu, W.-H., Lamarche, T., Dupuis, E., Jameux, D., Barnard, P., & Liu, G. (2013). Precision control of modular robot manipulators: The VDC approach with embedded FPGA. *IEEE Transactions on Robotics*, 29(5), 1162–1179.
- Zhu, W.-H., & Piedboeuf, J. C. (2005). Adaptive output force tracking control of hydraulic cylinders with applications to robot manipulators. *Journal of Dynamic Systems, Measurement, and Control*, 127(2), 206–217.
- Zhu, W.-H., & Vukovich, G. (2011). Virtual decomposition control for modular robot manipulators. In *Proc. IFAC world congress* (pp. 13486–13491).
- Zhu, W.-H., Xi, Y.-G., Zhang, Z.-J., Bien, Z., & De Schutter, J. (1997). Virtual decomposition based control for generalized high dimensional robotic systems with complicated structure. *IEEE Transactions on Robotics and Automation*, 13(3), 411–436.